Time-domain Kelvin Probe Force Microscopy for Local Ultra-Fast Decay Time Measurements

Thesis by

Zeno Schumacher

Department of Physics

McGill University, Canada

June 2016

Thesis submitted to McGill University in partial

fulfillment of the requirements of the degree of

Doctor of Philosophy

Acknowledgment

First and foremost, I would like to thank my supervisor Peter Grutter for giving me the great opportunity of working on this project. It has been a truly amazing journey that brought a lot of joy with it. Thank you!

Additionally, I would like to thank all my friends and lab mates who made my time in Montreal and in the lab awesome. In particular, big thanks to Jessica Topple and Antoni Tekiel for passing on their knowledge and teaching me all about the Jeol system and life in the basement. Thank you all, current and previous Grutter group members who had a significant impact on my life (no order intended): Jeff Bates, Andreas Spielhofer, William Paul, Antoine Roy-Gobeil, Ann-Lauriene Haag, Tyler Enright, Aaron Mascaro, Matt Rigby, Oscar Iglesias Freire, Xue Ying, Rasa Rejali and Monserrat Lopez, Katherine Cochrane.

Thank you, Yoichi Miyahara, for all your help with any challenges that I encountered.

I would also like to thank my family, Yalu, Fritz, Zoe, Cleo, Kreon and Keto, for supporting me on this adventure and for understanding that having fun with science is more important than earning a lot of money.

Lastly, I would like to thank my wife, Ann-Lauriene Haag, for always being there for me at home, in the lab and on top of all these mountains. I am grateful to have you!

Statement of Originality

The author, Zeno Schumacher, claims the following elements of this thesis to be considered original scholarship and distinct contribution to knowledge:

- A commercial ultra high vacuum atomic force microscope was updated with two ultrafast pulsed lasers.

- Development of a novel time-domain Kelvin probe force microscopy method for reliable and accurate measurement of surface photovoltage under pulsed illumination. The author points out that Kelvin probe force microscopy under pulsed illumination does not work as expected and a time-domain analysis method addressing this challenge is developed to measured the CPD. [Published: Z. Schumacher, et al. Phys. Rev. Applied 5, 044018, **2016**.]

- Measurement of local ultrafast decay constant in low temperature grown GaAs by atomic force microscopy (AFM). A non-degenerate optical pump-probe setup is integrated with a ultra high vacuum atomic force microscope. A general understanding for the measurement of ultrafast decay time measurement in AFM is developed. Measurement by AFM of time decays in the order of 1 ps are presented. [Presented in the

6th chapter of this thesis.]

- Studied the effect of gold coating thickness on cantilever Q-factor. The cantilever Q-factor is an important parameter determining the force and time resolution of AFM. Proposed a solution to prevent manufacturing limiting variation in coating thickness by using partially coated cantilevers. [Published: Z. Schumacher, et al. Beilstein J. Nanotechnol. 6, 1450-1456 , **2015**.]

- Contributed to a new method of KPFM using the dissipation signal in fm-AFM to measure the contact potential difference [Published: Miyahara, Y., Topple, J., Schumacher, Z., Grutter, P. Phys. Rev. Applied, 4(5), 054011, **2015**.

  Patent: US 20150276795 A1, **2014**]

Contribution of co-Authors

Chapter 5 is based on the following published manuscript:

Measurement of Surface Photovoltage by Atomic Force Microscopy under Pulsed Illumination

Zeno Schumacher, Yoichi Miyahara, Andreas Spielhofer, and Peter Grutter

Phys. Rev. Applied, **5**, 044018, **2016**

The author of this thesis conceived the measurement scheme and performed all the experiments and data analysis. Y. Miyahara assisted in preparing the manuscript. A. Spielhofer helped with system maintenance and proofread the manuscript. P. Grutter supervised the project and assisted in preparing the manuscript.

Abstract

Atomic force microscopy (AFM) was developed in the mid 1980's to measure the topography of a sample with atomic resolution. Since the first reported atomic resolution images, AFM has constantly been developed further to gain more insights into structure and property at the nanometer scale. Its great advantage is the capability to spatially resolve the tip-sample interaction at a sub-nanometer scale. Extensive research and development was conducted over the past two decades to not only measure the structure of a sample but also to extract information about the local properties. Kelvin Probe Force Microscopy is an example of such a technique, enabling the measurement of the local contact potential between the AFM tip and the sample.

In this thesis, AFM is used to spatially resolve the surface potential generated upon illumination of a sample with light. A new technique to accurately measure the change of the contact potential difference under pulsed illumination was developed and implemented. This new measurement technique was needed since we reached the limit of currently available methods. These did not allow the measurement of the surface photovoltage as a function of illumination wavelength or time. This new method allows a much more accurate determination of surface potential differences.

Resolving the surface photovoltage on a nanometer length scale with AFM can be of great interest in particular if one can additionally gain information about the temporal

response of the sample. To address this, we developed a method to study the decay of the surface photovoltage by non-contact AFM, which is only limited by the underlying physics process. The approach used to achieve fast time resolution measurements is discussed in a general context. We demonstrate that the well known fundamental sensitivity limits of force detection also govern the achievable time resolution. The time resolved methods developed in this thesis can be adapted to measure time resolved ion diffusion, thermal response and electronic pulse propagation. As a proof for the novel measurement method, the ultra-fast decay time of the photocarriers in low temperature grown GaAs of about 1 ps was measured by AFM. These experiments were implemented by combining a traditional optical pump-probe modulated excitation with localized readout by AFM, The spatial resolution is therefore given by the AFM setup and not the optical excitation.

Résumé

La microscopie à force atomique (MFA) a été développée dans le milieu des années 80 pour mesurer la topographie d'un échantillon avec une résolution atomique. Depuis les premières images de résolution atomiques obtenues, la MFA a constamment été amélioré pour raffiner notre compréhension des phénomènes à l'échelle du nanomètre. Son grand avantage est la capacité de résoudre le potentiel pointe-échantillon à cette échelle auparavant inaccessible. Davantage de recherche et de développement ont été réalisés au cours des deux dernières décennies pour mesurer non seulement la structure de l'échantillon, mais en plus d'extraire des informations sur les propriétés locales. Kelvin Probe Force Microscopy est un tel exemple, permettant la mesure du potentiel de contact local entre la pointe du MFA et l'échantillon.

Dans cette thèse, le MFA est utilisé pour résoudre spatialement le potentiel de surface générée lors de l'illumination d'un échantillon avec de la lumière. Une nouvelle technique pour mesurer avec précision le changement du contact différence de potentiel sous un éclairage pulsé a été développée et testée. Cette nouvelle technique de mesure est nécessaire pour repousser la limite des méthodes actuellement disponibles qui ne permettent pas de mesurer la phototénsion de surface en fonction de la longueur d'onde ou du temps d'illumination.

La résolution de la phototénsion de surface sur une échelle nanométrique avec le MFA peut être d'un grand intérêt, en particulier si l'on peut en outre obtenir de l'information sur la réponse temporelle de l'échantillon. Nous avons développé une méthode pour étudier

la diminution de la phototension de surface par MFA, limitée seulement par le processus physique sous-jacent. L'approche utilisée pour cette mesure de résolution temporelle est discutée dans un contexte général. Nous démontrons que les limites de sensibilité fondamentales de détection de force déjà établies régissent également la résolution temporelle réalisable par notre technique. Cela permet aux méthodes de résolution temporelle développées dans cette thèse d'être adaptées pour mesurer la diffusion d'ions dans le temps, la réponse thermique ainsi que la propagation d'impulsions électroniques par MFA. Comme preuve que la méthode de mesure proposée est viable, le temps de décroissance de photoporteurs dans un matériau de GaAs préparé à basse température, d'environ 1 ps, a été mesuré par MFA. Ces expériences ont réalisées en combinant une excitation optique traditionnelle de type pompe-sonde avec lecture localisée par le MFA. La résolution spatiale est donc déterminée par le MFA et non l'excitation optique.

Contents

1

Introduction

Atomic force microscopy (AFM) was developed by Binnig, Quate and Gerber to measure the topography of insulating samples with atomic resolution in 1986 [1]. AFM measures the tip-sample force in contrast to the earlier invented scanning tunneling microscopy which measures the tunneling current [2]. Various modes of AFM exist, such as contact mode, frequency modulation and amplitude modulation [3]. A tip with a radius of a few to tens of nanometers is attached to a mechanical oscillator, often a cantilever. The change in the state of the oscillator, such as deflection, change in frequency or amplitude, due to the interaction of the nanometer size tip with the sample, is record. The tip is scanned over the surface to generate a topographic map of the sample with a spatial resolution given by the tip radius.

More research and development was conducted to not only measure the topographical structure of samples at the nanometer scale, but to extract information about their local

properties. In 1991, this lead to the development of Kelvin probe force microscopy (KPFM) by Nonnenmacher et al. [4]. KPFM is a scanning probe variation of the macroscopic Kelvin probe method established by Lord Kelvin in 1898, to measure the local contact potential difference between two materials [5]. KPFM uses an oscillating voltage between the AFM tip and the sample to modulate the electostatic force. A feedback loop can be used to find the minimum of the electrostatic interaction [6]. By recording this minimum while scanning the tip over the surface, a map of the local surface potential is obtained. KPFM was soon used to study semiconductors under illumination with light to measure the surface photovoltage [8]. The surface photovoltage is measured as the change of the KPFM signal (e.g. contact potential difference) under illumination. It is therefore often used to study photovoltaic materials. These techniques are the building blocks to study the structure-function relationship of photoactive materials with AFM [9–20, 14].

Frequency modulated AFM (fm-AFM) was first presented by Albrecht et al. in 1991, allowing AFM applications in vacuum [7] . In fm-AFM, the frequency shift of the cantilever is measured rather than the change in amplitude, allowing for easy operation of high Q-factor cantilevers under ultra high vacuum condition with increased sensitivity.

1.1 Motivation

Organic photovoltaic materials (OPV) have been intensively studied in the last 15 years [21, 10, 22–24]. Research on OPV has shifted from finding new materials with higher efficiencies to understanding the fundamental processes during charge generation [23, 25–27]. In organic semiconductors, absorption of photons leads to the creation of bound electron-hole pairs (Frenkel excitons), in contrast to the free electrons and holes created in inorganic semiconductor photovoltaic devices. The spatial dimension of a Frenkel excitons in an organic systems is on the order of a few nm (i.e. the size of the molecule) due to the very small dielectric constant of organic materials compared to semiconductors. These excitons carry energy, but no net charge, and therefore, have to separate into holes and electrons on separate molecules, before the charge can be collected at an electrode and thus generating a current. The process of charge transfer from the locally bound exciton to the free charges on two different molecular species involves various molecule specific pathways as well as trap states. The current proposed scheme in organic photovoltaics is that the generated exciton will first form a charge transfer state (CT state) [26, 28]. This CT state is still a Coulomb bound electron-hole pair, however, it might be delocalized across multiple molecules in contrast to the previously generated Frenkel exciton. A CT state can dissociate into free charges, which can then diffuse to the electrode to be collected. A graphical summary of the excition

generation, CT state and separated charge state is shown in figure 1.1.

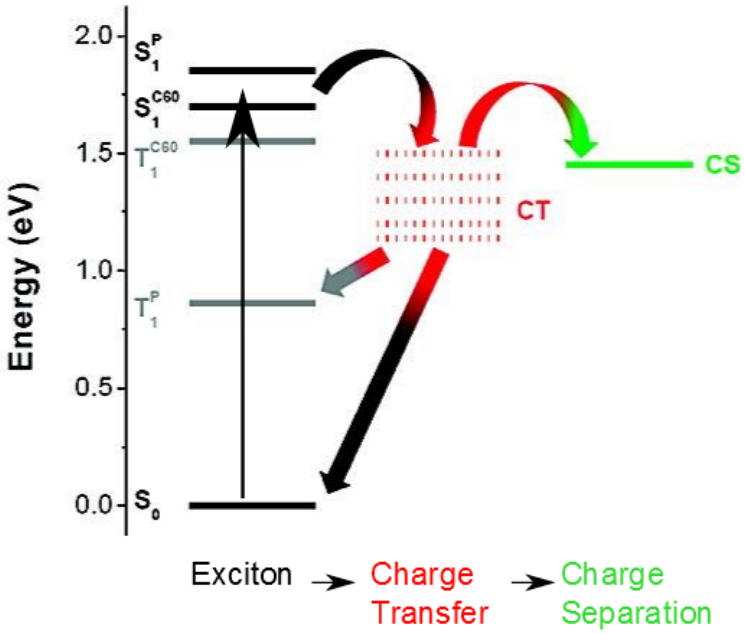

Figure 1.1: Illustration of the charge separation process in organic solar cells. An excition is generated upon adsorption (black). The exciton can dissociate into free charges (CS, green) via a charge transfere state (CT, red). The charge transfere state can also recombine. Figure reprinted (adapted) with permission from Yi, et al., Journal of the American Chemical Society [29]. Copyright 2009 American Chemical Society.

Most research has focused on measuring the timescales associated with the involved processes [30, 31]. For process faster than a nanonsecond this is often done optically with ultrafast pulsed lasers, which can generate laser pulses below 100 fs. The spatial characterization of organic solar cells is challenging, but is needed in order to understand details of the structure-function relationship such as the role of defects. Solution processed samples and

films exhibit a high density of defects. All processes involved in the charge separation have associated rates and competing pathways, e.g. due to recombination sites or charge traps. These competing pathways reduce the charges available at the electrodes and can reduce charge mobility by acting as a scattering center and thus the amount of current a device can produce for a given photon flux (i.e. efficiency). It is well accepted that the morphology of organic films play an important role for these pathways, leading to the engineering of structures based on the phase separation of different functional components [26, 31]. Such structures are for example bulk heterojunctions. These consist of a mix of donor and acceptor molecules forming interfaces throughout the device in contrast to a planar two layer structure. Bulk heterojunctions are the preferd device form for many molecule systems to-date [24]. The detailed role, in particular, the importance and nature of defects relevant for the different processes, however, remain elusive due to a lack of experimental techniques capable of determining the structure-function relationship in OPV materials at the relevant molecular length scale. This is an important missing next step not only from a fundamental point of view but also to guide improvements in efficiency and stability of OPV in solar energy conversion, which is a major interest for research to-date [24].

Currently, only a few tools are available to investigate the structure-function relationship in OPVs at a molecular (nano)-scale. Particularly powerful is the combination of Kelvin Probe Force Microscopy (KPFM) to observe charge distribution and non-contact Atomic

Force Microscopy (nc-AFM) to simultaneously obtain structural information [11, 9, 13, 15]. This allows for the investigation of structure-function relationships in organic photovoltaics at the relevant nanometer level. Molecular defects, Frenkel excitons and charge transfer states are all occurring at these lengths, as mentioned above.

In 2005, Hoppe et al. presented a study of KPFM on conjugated polymer/fullerene bulk heterojunction organic solar cells and thus showed a change in KPFM under illumination [16]. Burke et al. presented preliminary results of PTCDA molecules adsorbed on a NaCl substrate with AFM and KFPM in 2009, where only bulk-like crystals structures showed significant change in CPD under illumination [11]. In 2006, Coffey and Ginger presented a time-resolved electrostatic force microscopy study on polymer solar cells and the local photoinduced charging in the milisecond range [9]. Henning et al. presented a KPFM study of nanocrystaline TiO_2 photoelectrodes and found spatial inhomogeneities in the micrometer scale [13]. All of these studies showed the great capability of AFM to locally measure the effect of illumination on organic semiconductors. However, these are either static measurements offering no time resolution or time resolution in the millisecond range. The process of charge generation can occur on time scales as fast as femtoseconds [26, 30]. A first fast time resolution was achieved in 2015 by Jahng et al by using the photo-induced force microscopy and an ultrafast laser to measure the dynamics in silicon naphtalocyganine [32]. Photo-induced force microscopy relies on a force generated by the light-induced dipoles in the tip

and sample. This indicates a great potential of extending AFM capabilities to measure fast processes. However, due to the need of a photo-induced tip dipole, Jahng's method can not be adapted easily.

The aim of this thesis is to develop tools for a better understanding of the structure-function relationship in OPV materials at the molecular scale. A new technique based on nc-AFM and KPFM with pulsed laser illumination is developed. Nc-AFM and KPFM can be used to study the structure and charge distribution in OPV materials, respectively. KPFM measures the surface potential difference (i.e. work function difference) between the sample and the tip of the AFM. A change in the energy level of the sample (molecules under illumination) can, therefore, be detected. However, KPFM is currently lacking the time resolution needed to study the charge generation process in OPV. The usual time resolution of KPFM lies at best in the tens of milliseconds. It can, therefore, be used to study the difference in OPV materials with and without illumination but so far cannot resolve the processes that happen during the charge generation, as these happen on a much faster timescale (i.e. <nanoseconds).

This thesis is structured as follows. First, an overview of the experimental methods is given in chapter 2. In particular, our measurement techniques (AFM, KPFM, etc.) are described in more detail. In chapter 3, a complete description of the experimental setup is presented. Chapter 4 illustrates a measurement of the surface photovoltage on organic

molecules in ultra high vacuum. The presented data is used to illustrate the challenges associated with the current surface photovoltage measurement technique and motivates the need for a new measurement technique.

Based on the results from chapter 4, a new technique to measure the change of the contact potential difference under pulsed illumination was developed and tested. Chapter 5 introduces this new technique using a time-domain analysis of the electrostatic force under pulsed illumination. The advantages over a traditional surface photovoltage measurement are highlighted and illustrated by a measurement on a silicon sample.

In chapter 6, the time resolution of AFM is discussed. Resolving the surface photovoltage spatially with AFM as well as information about the temporal response of the sample are of great interest. Therefore, we developed a method to study the decay of the surface photovoltage by non-contact AFM which is limited only by the underlying physical processes. We demonstrate the capability of this approach by measuring the $\sim$1 ps photo excitation decay time of a low-temperature grown gallium arsenide sample. The approach used for this time resolution measurement is discussed in general terms, allowing it to be adapted for the use of other time-varying signals in nc-AFM such as ion diffusion, thermal response, and electronic pulse propagation.

2

Experimental Methods

In the following chapter the theory for non contact Atomic Force Microscopy (nc-AFM) and Kelvin Probe Force Microscopy (KPFM) will be discussed.

2.1 Non Contact Atomic Force Microscopy

nc-AFM is a variation of AFM where the tip sample interaction is measured without establishing mechanical contact between the tip and the sample. Nc-AFM is often interchanged with frequency-modulated AFM (fm-AFM), since nc-AFM is predominantly used in frequency modulation mode. In fm-AFM a cantilever is oscillating at its resonance frequency and the deviation of the frequency due to the tip-sample interaction is measured. The cantilever can be expressed as a damped driven harmonic oscillator:

$$m\ddot{z} + \frac{m\omega_0}{Q}\dot{z} + kz = F_{\text{drive}}(t) + F_{\text{ts}}(z,t), \tag{2.1}$$

where k is the spring constant, Q the quality factor, m the effective mass of the cantilever, z the position of the tip with respect to the equilibrium position. The Q-factor of AFM cantilever can be effected by the reflective coating on the backside. A small fluctuation of a few nanometer coating thickness can lead to a sigificant reduced Q-factor. We presented a study about this effect and proposed a partial coating as a possible solution [33].

A feedback loop is driving the cantilever at its resonance frequency by compensating any energy losses. Therefore, under ideal conditions the driving force F_{drive} and the damping term can be neglected, and equation 2.1 can be written as [34]:

$$m\ddot{z} + kz = F_{\text{ts}}(z,t). \tag{2.2}$$

In the small amplitude limit, valid when force gradient is small compared to the amplitude (e.g. $d^2F/dz^2 \sim 0$), the interaction force can be linearized in z and an analytical expression for the frequency shift Δf can be obtained:

$$\Delta f \cong -\frac{f_0}{2k}\frac{\partial F_{ts}}{\partial z} = \frac{f_0}{2k}\frac{\partial^2 U_{ts}}{\partial z^2}. \tag{2.3}$$

From equation 2.3 it can be seen that the measured frequency shift is proportional to the force gradient and not the force. This was mentioned in the original fm-AFM publication

in 1991 [7]. It was noted that the frequency of the cantilever is given by $f = 1/2\pi\sqrt{k_{\text{eff}}/m}$ with the effective spring constant given by $k_{\text{eff}} = k + \partial F/\partial z$.

For larger amplitude operation, perturbation theory or other approaches need to be used to solve the equation of motion [34, 35]. In general, the frequency shift is related to the average of the tip sample force F_{ts} during a full cantilever oscillation [3]:

$$\Delta f = -\frac{f_0}{kA_0^2}\langle F_{ts}\rangle = -\frac{f_0}{kA_0^2}\frac{1}{T_0}\int_0^{T_0} F_{ts}[d + A_0 + A_0\cos(2\pi f_0 t)]A_0\cos(2\pi f_0 t)dt. \tag{2.4}$$

with d the distance of closest approach. The frequency shift for large amplitudes does depend on the operating condition, such as the amplitude A_0 and the cantilever characteristics (spring constant k and resonance frequency f_0).

2.1.1 Interaction Force in nc-AFM

The tip sample force measured in nc-AFM is a sum of different long and short range forces. Three relevant forces for nc-AFM can be distinguished: van der Waals, electrostatic and chemical forces.

The **van der Waals** force is given by

$$F_{vdW} = -\frac{HR}{6z^2}. \tag{2.5}$$

The tip sample geometry is approximated as a sphere close to a flat surface, with R

the tip radius, z the tip-sample distance and H the Hamaker constant (material dependant parameter).

For high resolution imaging the variation in **chemical forces** due to wave function overlap or Pauli repulsion are measured. The Morse potential can be used to describe the chemical forces. Due to their very short interaction range, they significantly contribute to the atomic contrast.

The **electrostatic force** arises from the different work function and applied electric potentials between the tip and the sample and the tip-sample capacitance. The difference in work function leads to a contact potential difference (CPD). The electrostatic force can then be written as:

$$F_{elec} = -\frac{1}{2}\frac{\partial C}{\partial z}V^2 \quad \text{with} \quad V = V_{\text{ts}} - V_{\text{CPD}}, \tag{2.6}$$

where C is the tip-sample capacitance, V_{ts} is a bias voltage applied between the tip and the sample, and V_{CPD} is the voltage corresponding to the contact potential difference. The capacitance is geometry dependent and can be approximated with a model of a sphere in close proximity ($z \ll R$) to a planar surface:

$$C = \frac{\pi\epsilon_0 R}{z}. \tag{2.7}$$

The contribution of the electrostatic force to AFM measurements is extensively used in this thesis and will be discussed in more detail in the following section.

2.1.2 Nc-AFM Feedback Loop

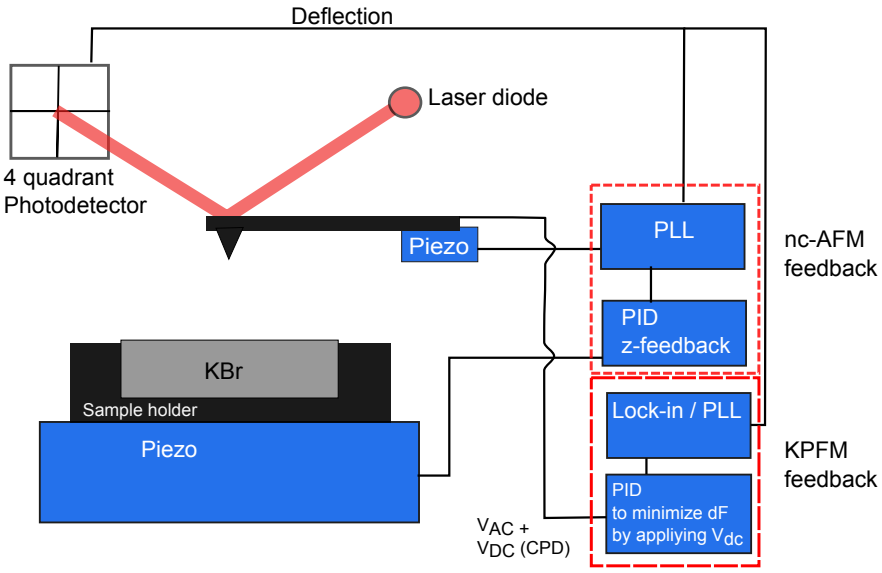

Figure 2.1: Block diagram of the feedback loop for nc-AFM and KPFM operation. The nc-AFM loop consists of a PLL and PID controller keeping the cantilever at a constant frequency shift. The KPFM feedback loop uses a lock-in and a DC-bias to minimize the electrostatic force modulated by V_{AC}

To operate at a constant frequency shift, a feedback loop with a proportional-integral-derivate (PID) controller is used. The cantilever is driven by a piezo at its resonance frequency. A phase lock looped (PLL) is used to adjust the drive frequency, as mentioned above. A constant frequency shift is then used for the z-feedback loop. The z-feedback loop consists of a piezo that is used to control the tip-sample distance in order to maintain the setpoint. The change in piezo position is recorded and used as the topography signal. In a x,y,z cooridnate system, z is usually referred to as the direction perpendicular to the sample

surface (x/y plane). A block diagram of the feedback loop is shown in figure 2.1. Various aspects of the feedback loops, such as the PID and PLL settings, the z-controller and time constant considerations for each loop are discussed in depth in literature [36, 37]. However, one useful relation between scanning speed and minimal bandwidth is worth mentioning here. The minimum distance, d_0, between features to be resolved together with the scanning speed, v_s, can be converted to a frequency. Hence the minimum bandwidth needs to include this frequency:

$$BW_{min} = \frac{v_s}{d_0}. \tag{2.8}$$

Especially for atomic resolution, which is a periodic structure, this relation is useful to keep in mind, so that the bandwidth is not set too low or the scan speed too high, which would result in poor resolution of the atomic structure.

2.2 Kelvin Probe Force Microscopy

Kelvin Probe Force Microscopy is based on the principle of measuring the contact potential difference introduced by Lord Kelvin in 1898 [5]. It was adapted for use with scanning probe techniques in 1991 by Nonnemacher et al. [4] and Weaver et al. [8]. As mentioned above, the contact potential difference (CPD) arises from different work functions between the tip and the sample when they are in electric contact, as illustrated in figure 2.2. For

KPFM sometimes it is also referred to as the local contact potential difference (LCPD), due to the high spatial resolution. When two metals come into electrical contact, charge flows between the two materials to align the Fermi levels. The new charge distribution leads to the establishment of an electric field between the tip and the sample. A DC bias can be applied to counter the charge redistribution and therefore nullify the electric field. The applied DC bias is equal to the contact potential difference when the electric field is compensated.

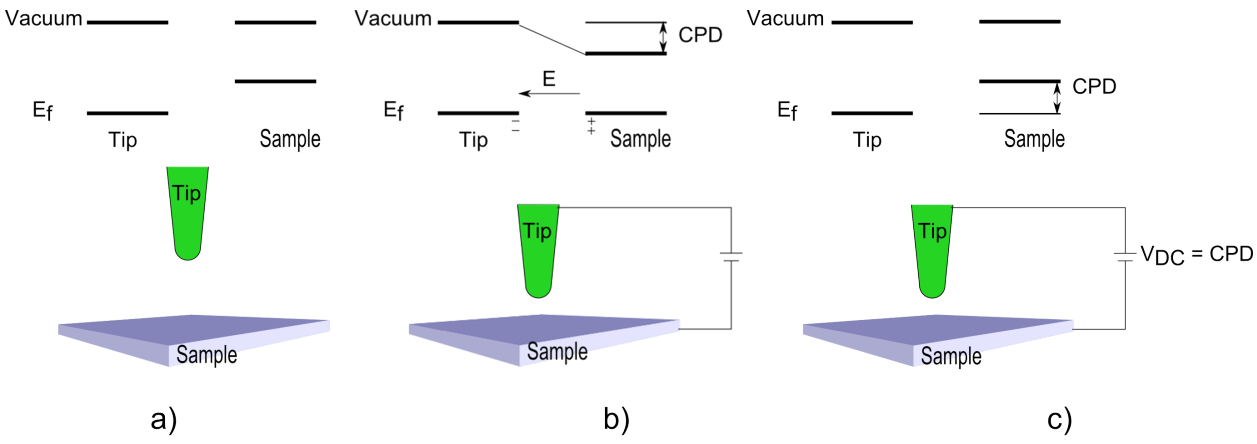

Figure 2.2: Principle of KPFM illustrated with two metals. (a) Tip and sample are not electrically connected, no electric field is present. (b) When the AFM tip is electrically connected to the sample, the Fermi levels align, resulting in an electric field between the tip and the sample. (c) By applying a bias between the tip and the sample, the vacuum levels are aligned again, thus the electric field vanishes. The applied bias is equal to the local contact potential difference (LCPD).

The frequency shift dependence on the applied bias according to $\Delta f_e \propto -\frac{1}{2}\frac{\partial^2 C}{\partial z^2}(V_{\mathrm{DC}} - V_{\mathrm{CPD}})^2$ can be measured by bias spectroscopy [38]. The tip is held at a constant tip sample distance

while the bias is swept and the resultant change in frequency shift is recorded. Such a frequency shift-bias curve can be seen in figure 2.3. When the measured data is fitted to the above mentioned equation, the CPD as well as the capacitance second derivative can be recovered. The maximum of the parabola gives the CPD and the curvature holds information about the second derivative of the capacitance.

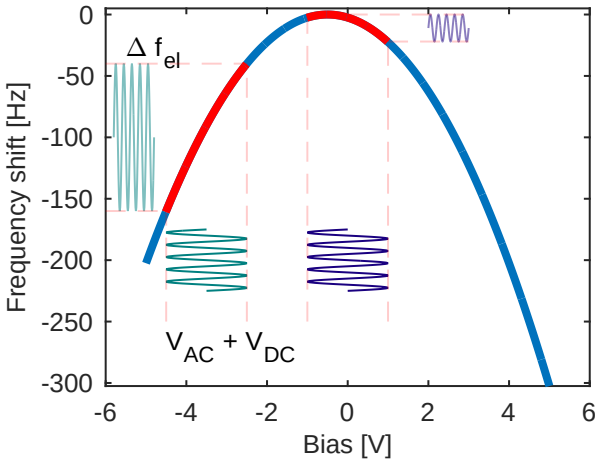

Figure 2.3: Bias spectroscopy at constant tip sample distance. The Kelvin parabola is recovered following equation 2.6. The principle of KPFM is illustrated by the applied AC-voltage, which results in a Δf modulation. By adjusting the DC-bias the frequency shift modulation can be minimized.

In KPFM an AC-voltage V_{AC} is applied to modulate the electric force. Including this AC-term into equation 2.6, the electrostatic force is described as:

$$F_{\mathrm{el}} = -\frac{1}{2}\frac{\partial C}{\partial z}((V_{\mathrm{DC}} + V_{\mathrm{ac}}\sin(\omega_{\mathrm{ac}}t)) - V_{\mathrm{CPD}})^2. \tag{2.9}$$

This modulation leads to three components of the electrostatic force at different frequen-

cies assuming no uncompensated (trapped) charges are present in the tip or sample:

$$F_{\mathrm{el}} = F_{\mathrm{DC}} + F_{\omega_{\mathrm{AC}}} + F_{2\omega_{\mathrm{ac}}}, \tag{2.10}$$

with

$$F_{\mathrm{DC}} = -\frac{1}{2}\frac{\partial C}{\partial z}((V_{\mathrm{DC}} - V_{\mathrm{CPD}})^2 + \frac{1}{2}V_{\mathrm{ac}}^2), \tag{2.11}$$

$$F_{\omega_{\mathrm{ac}}} = -\frac{\partial C}{\partial z}((V_{\mathrm{DC}} - V_{\mathrm{CPD}})V_{\mathrm{ac}}\sin(\omega_{\mathrm{ac}}t), \tag{2.12}$$

$$F_{2\omega_{\mathrm{ac}}} = -\frac{1}{4}\frac{\partial C}{\partial z}V_{\mathrm{ac}}^2\cos(2\omega_{\mathrm{ac}}t). \tag{2.13}$$

This modulation of the electrostatic force at the frequency ω_{ac} or $2\omega_{\mathrm{ac}}$ can again be measured by amplitude modulation or frequency modulation. Here we will focus on the case of frequency modulation. Each of these forces will result in a frequency shift at the corresponding frequency, ω_{ac} and $2\omega_{\mathrm{ac}}$ since $\Delta f_{\omega_{\mathrm{ac}}} \approx \partial F_{\omega_{\mathrm{ac}}}/\partial z$. The applied frequency $f_{\mathrm{ac}} = \omega_{\mathrm{ac}}/2\pi$ is usually between a few hundred Hz to a few kHz. This low frequency modulation will result in a modulation of the frequency shift at the cantilever resonance frequency, e.g. a sideband at applied frequency $f_0 \pm f_{\mathrm{ac}}$. This is equivalent to FM radio, where a carrier f_0 is modulated by f_{ac}. There are two main techniques used for the measurement of

the KPFM signal, a tandem lock-in setup and a direct sideband detection. A block diagram for both detection methods can be seen in figure 2.4.

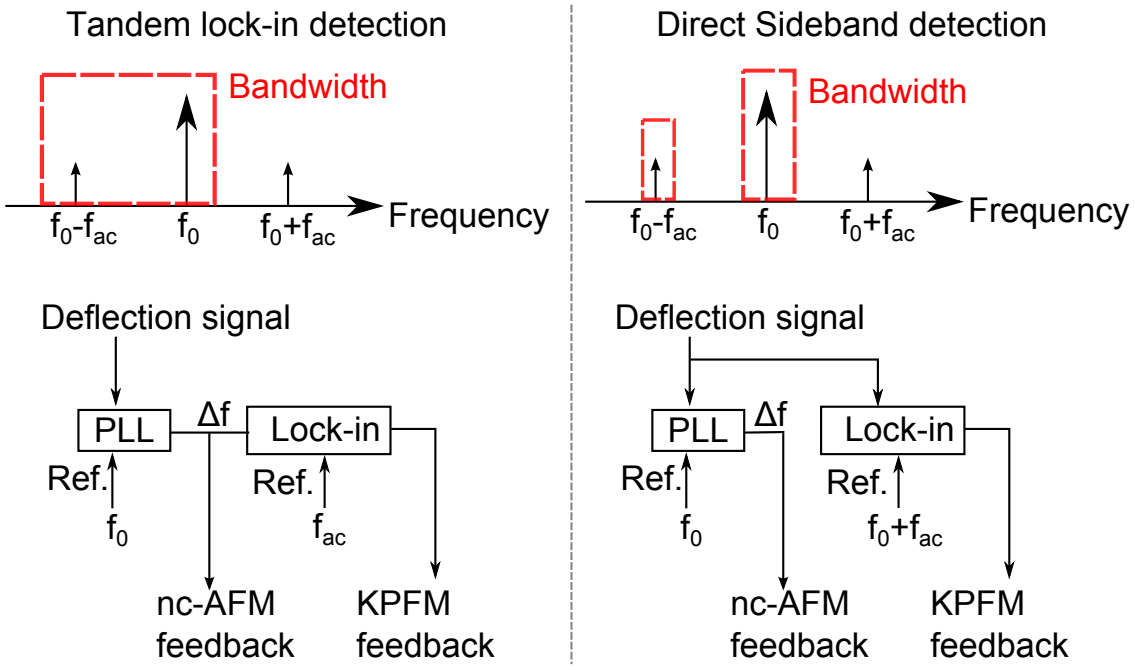

Figure 2.4: Tandem lock-in detection compared to direct sideband detection. For tandem measurements the bandwidth (red) of the PLL needs to be high enough to include the modulation. Direct sideband detection allows to choose the bandwidth for the carrier f_0 (cantilever resonance) and modulation f_{ac} independent.

One approach to demodulate these signals is to use a tandem set-up with two lock-in amplifiers. The first lock-in is part of the nc-AFM feedback and measured the cantilever frequency shift signal including the f_{ac} modulated signal. A second lock-in is used with this signal as an input to measure the effect of V_{ac} at frequency f_{ac}. To be able to measure

this modulation the bandwidth of the first lock-in/PLL needs to be set high enough to not attenuate the KPFM signal. However, since the same Δf signal is used for the z-feedback, a low bandwidth is desired for signal-to-noise purposes. Hence, a trade-off between signal strength of the KPFM signal and noise in Δf needs to be taken into account.

To prevent the high bandwidth on the PLL responsible for the z-feedback, a direct sideband detection can be used. Direct sideband detection is a lock-in technique where the carrier and sideband modulation are directly measured, independent from each other. The Zurich Instruments lock-in amplifier (HF2) includes this easy to use option (MOD-option). Two demodulators are used, one operating at the carrier frequency (in our case the cantilever oscillation f_0) and a second modulator at the frequency of the sideband (f_{ac}). The measurement signal is then digitally demodulated at frequencies f_0, $f_0 + f_{\mathrm{ac}}$ and $f_0 - f_{\mathrm{ac}}$, each with their own bandwidth setting. This allows an optimal bandwidth on the frequency shift channel as well as on the KPFM signal.

Independent of the type of measurement, a feedback loop is used to adjust the applied DC voltage to minimize the signal strength at frequency f_{ac}. When the signal is minimized, the applied DC-bias is equal to the contact potential voltage, $V_{\mathrm{DC}} = V_{\mathrm{CPD}}$. Hence, the DC-bias is recorded to map the contact potential difference when the AFM probe is scanned over the surface.

The DC term in equation 2.11 will lead to an offset proportional to the square of the

amplitude of the AC voltage, since the first term vanishes when the DC voltage compensates the contact potential difference. To correct for this offset, the frequency shift set-point of the nc-AFM feedback can be adjusted to reduce the tip-sample separation. The signal at $2\omega_{ac}$ (equation 2.13) can be recorded as well to gain insight in the tip-sample capacitance. However, an additional lock-in amplifier is needed to perform this measurement.

One should note that KPFM is not only useful in measuring the distribution of the contact potential, but also in determining the true height of surface features [39]. Different materials on a surface (adsorbed molecules, step edges) will result in a change in electrostatic force. This will result in a frequency shift that can be mistaken for a change in topography. Therefore, KPFM is often used to assure the true height is measured. An example of such a false measurement can be seen in figure 2.5. A cleaved Potassium Bromide (KBr) sample is measured with AFM only (cross-section 1) and with the addition of KPFM (cross-section 2). One can see that the topography changes as soon as the KPFM feedback loop is turned on. The step edge in KBr exhibits a different CPD than the terrace, which is to be expected due to the different potential at the step edge and possible trapped charges [40, 41]. Due to the difference in CPD the step appears at the wrong height when measured without KPFM. As soon as KPFM is used a height of 0.34 nm is measured, in agreement with previously reported values by AFM [42].

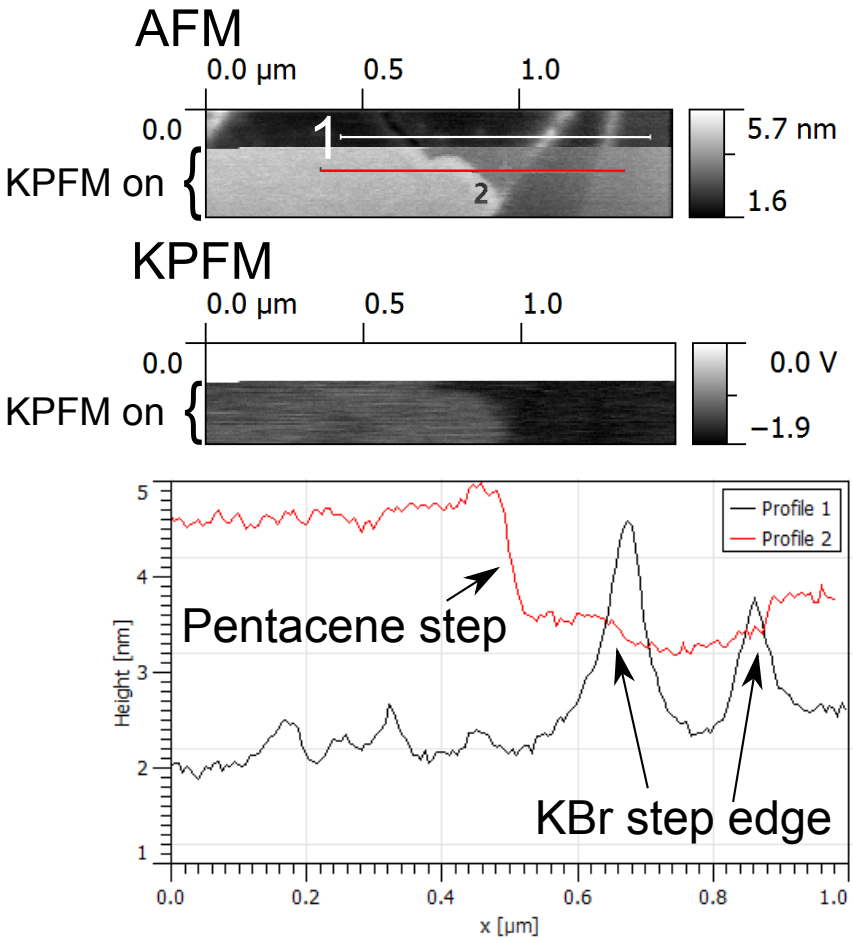

Figure 2.5: AFM image of cleaved KBr with adsorbed pentacene, with and without KPFM. The top of the image is recorded with no DC-bias applied to the tip. For the lower part of the image, the KPFM feedback loop is turned on and a KPFM contrast is visible. The height profile show the effect of KPFM in the topography image. The step edge and the edge of the molecule island only appear at the correct height when the KPFM feedback is on. The step edge does not appear as a step but more like a line without KPFM. This is due to trap charges at the step edge. A plane subtraction was used for the topography image.

2.2.1 Spatial Resolution

The spatial resolution of KPFM depends on the tip geometry and the tip-sample distance z. In first approximation it can be assumed that the spatial resolution is about the tip-sample distance when the tip-sample distance is larger than the tip radius r_{apex}. For a closer approach measurement, when $z < r_{apex}$, the resolution is given by about the tip radius r_{apex} [43]. Gross et al. presented a nice analysis for functionalized tips and concluded that the main contribution stems from the electrostatic force [44]. This confirmed appropriate tip structures can yield atomic resolution in KPFM.

The penetration depth and therefore the resolution into the sample is, however, not yet well understood [45]. It does highly depend also on the sample capacitance and the applied field. Therefore estimating the probe depth of KPFM is not a trivial task.

Also one should note that the cantilever itself can contribute to the overall measured electrostatic force in KPFM, basicly adding a background offset to it [46, 47].

2.2.2 Surface Photovoltage

Surface photovoltage (SPV) refers to the change of CPD under illumination [48–50]. A typical measurement of surface photovoltage consists of two KPFM measurements [14, 17, 16, 51–54]. The first measurement is performed under dark conditions to obtain the CPD of the material. Then the KPFM measurement is repeated under illumination to measure

the CPD under illumination. The difference between the two measurements is referred to as the surface photovoltage SPV = $\mathrm{CPD}_{\mathrm{dark}} - \mathrm{CPD}_{\mathrm{illumination}}$. The CPD can be measured by KPFM or bias spectroscopy. KPFM possess the advantage of collecting information about the distribution of the CPD across the surface compared to a point measurement by bias spectroscopy. However, if KPFM images are used to determine the SPV, any spatial drift needs to be taken into account before subtracting the images to not include any artifacts created by a spatial shift. Commonly neglected but equally important, one needs to ensure that the tip CPD does not change during the two measurements.

3

Material and Methods

A JEOL 4500A UHV AFM was used for all studies in this thesis. The AFM and the optical setup will be explained below, followed by a more detailed description of the combination of the laser illumination to the UHV chamber.

3.1 UHV AFM Setup

A commercial JEOL 4500A UHV AFM was used with various custom modifications. The UHV system consists of a preparation chamber, a measurement chamber and a load lock. A picture of the system can be seen in figure 3.1. The preparation chamber includes various instruments for surface science preparation. Both chambers are evacuated using each an ion pump (Satsuki SIP-300XH-T16) with a pumping speed of 300 L/s for N_2 and a Ti sublimation pump (ULVAC PGT-3F, 1600 L/s for N_2). A base pressure in the low 10^{-11} mbar can

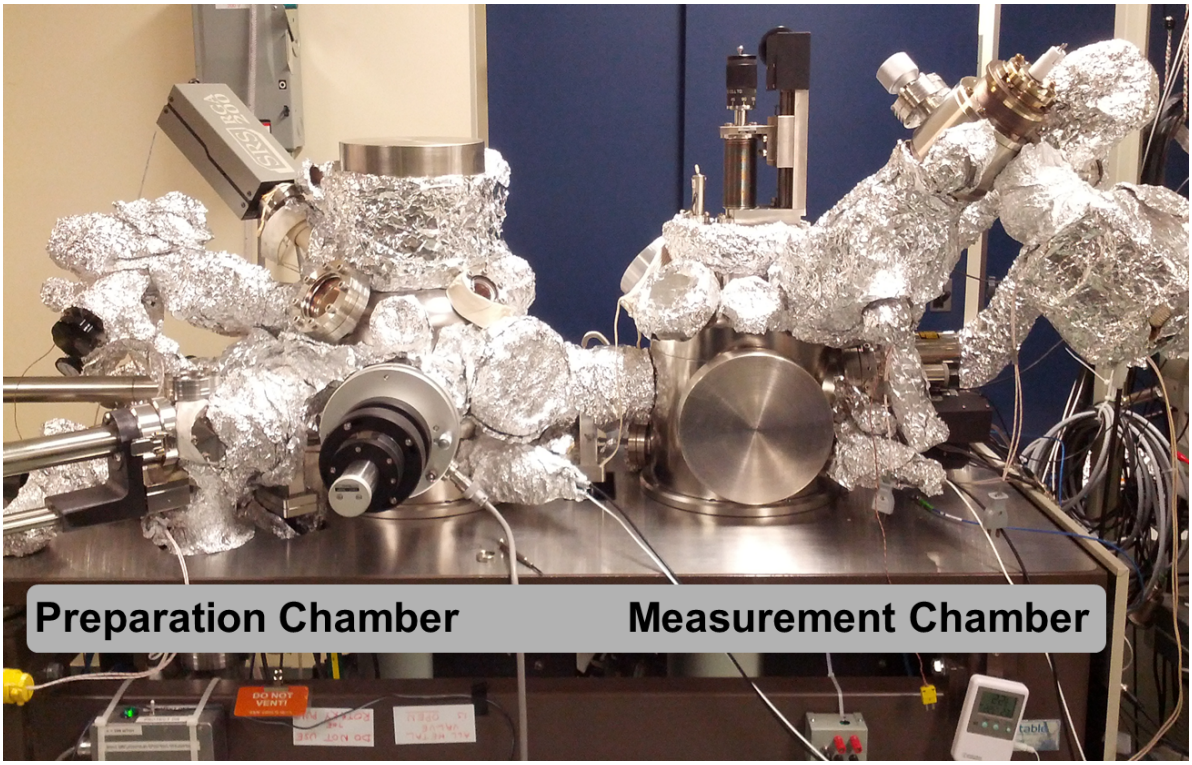

Figure 3.1: JEOL 4500A UHV AFM. The system has a preparation chamber and a measurement chamber hosting the AFM. An SEM is attached to the measurement chamber.

be maintained in the preparation chamber, whereas the base pressure in the measurement chamber reaches 3×10^{-10} mbar; this degradation in vacuum quality is due to the scanning electron microscope (SEM) attached to the measurement chamber. A turbo-molecular pump (Pfeiffer TMU261, 210 L/s for N_2) is attached to the load lock. This allows for an easy exchange of AFM tips and sample after a short ($\sim$ 6 hours) bake of the load lock. The turbo-molecular pump is backed by a rotary pump (Adixen 2010SD, 9.7 m^3/hr). During AFM measurement the turbo-molecular pump is turned off to reduce vibrations. The UHV

chambers are mounted on a vibration isolating air table for further damping. The load-lock and the preparation chamber each have a magnetically coupled rotating linear transfer arm for sample and tip transfers between the chambers. Furthermore, the preparation chamber hosts a carousel that can hold up to three sample holders and one tip holder. An additional sample storage was installed in the measurement chamber, which is capable of holding up to 3 samples. In the preparation chamber, the cleaving station was used for *in situ* cleaving of alkali halides (KBr and NaCl) to ensure that the surface of the sample is not been exposed to air prior to measurements. A three pocket Knudsen cell evaporator (Kentax TCE-BSC) was used for molecule deposition on cleaved alkali halides.

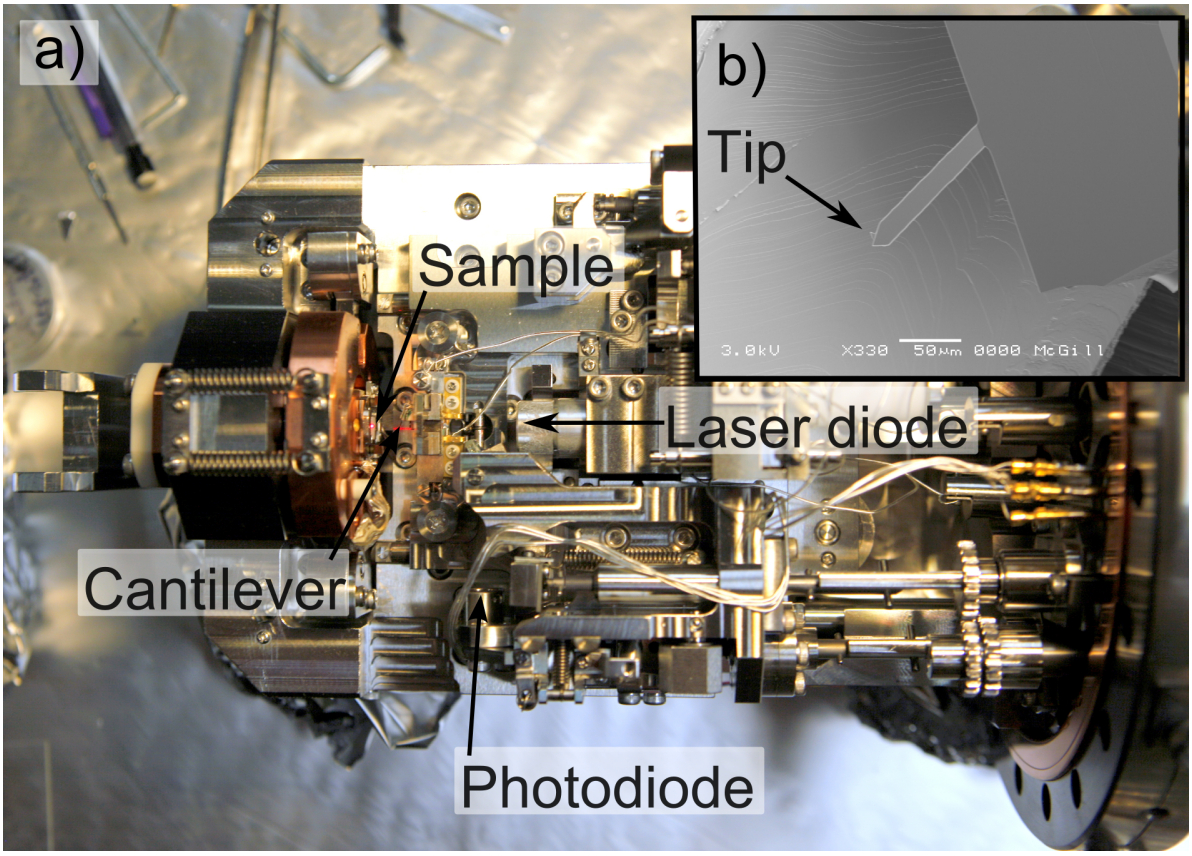

Figure 3.2: a) JEOL AFM head. The cantilever, sample, laser diode and four quadrant photodiode are indicated by arrows. b) SEM image of the AFM cantilever in front of a cleaved KBr sample. The AFM tip is visible.

The measurement chamber holds the AFM stage, as well as a scanning electron microscope (SEM). A picture of the AFM stage can be seen in figure 3.2. The entire AFM stage is spring loaded for damping purposes. The cantilever holder can be mechanically retracted for the sample/tip exchange. When the cantilever holder is placed towards the sample, it is locked in placed with the sample stage.

3.2 Optical Ultrafast Pulsed Laser Setup

The optical pulsed laser setup consists of two fiber-based ultrafast pulsed lasers. A picture of the optical setup is shown in figure 3.3. A FemtoFiber Pro near infrared (NIR) ultrafast fiber laser with an output of $>$ 360 mW at 1560 nm is used as the first laser. A nonlinear crystal for second harmonic generation can be used to generate a 780 nm output wavelength with a power of 192 mW. The pulse width is 94 fs for both outputs. A second laser is a FemtoFiber pro tuneable visible (TVIS). This version allows for the generation of sub-picosecond pulses (0.4 ps) at wavelengths between 480 nm to 640 nm. A supercontinuum is generated in a highly nonlinear fiber, pumped by the base frequency of 1560 nm. A manually tunable second-harmonic generation crystal is used to generate the desired output wavelength. The average output power varies between 2.4-19 mW depending on the wavelength. Both systems have a repetition rate of 80 MHz. The FemtoFiber pro NIR laser includes a variable repetition rate option and a phase-lock loop laser synchronization electronics. These options allow for locking the laser to the repetition rate of the tunable laser. A jitter of below 100 fs is achieved under stable lock conditions. Furthermore, these options allow for the introduction of a temporal delay between the two lasers ($\pm$250 ps) through applying a constant phase offset to the synchronization electronics.

An optical delay stage (Thorlabs DDS220) is used to further delay the two lasers with

respect to each other when the electronic delay mentioned above of ±250 ps is not sufficient. A 25.4 mm clear aperture retroreflector (Edmund Optics # 46-183) is mounted on the delay stage to facilitate alignment. A longpass dichroic mirror with a cutoff wavelength of 650 nm (Thorlabs DMLP650T) is used to combine the two beams. A mechanical chopper system (Thorlabs MC2000) can be used to modulate the laser beam. A ten slot blade is used for most experiments, allowing for the selection of frequencies between 20 Hz to 1 kHz.

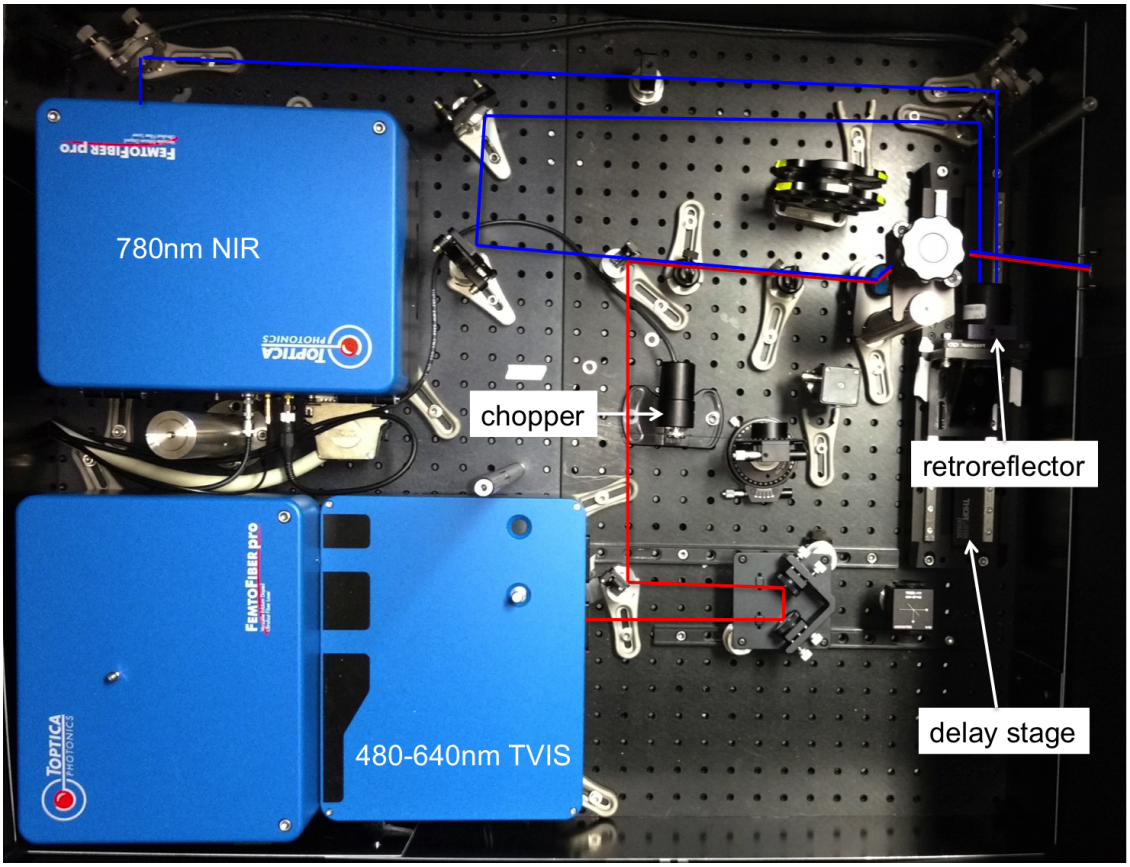

Figure 3.3: Picture of optical table with laser setup including delay stage and chopper. Beam path is shown in red (TVIS) and blue (780nm) for guidance only, no accurate angles.

3.3 Integration of fs-Laser System to a Commercial UHV AFM Setup

For experimental purposes, our commercial UHV AFM setup needed to be modified to allow illumination of the tip sample gap with a pulsed laser source. The AFM setup placed several constraints to the necessary integrations. First of all, the AFM head itself should not be modified, so as to not compromise the stability of the setup, and to have less downtime during modification. The laser should not be fixed to the vibration isolated table so that the mechanical vibrations are not coupled. Furthermore, geometrical constrains are given by the design of the AFM head and the position of the cantilever relative to the sample. The cantilever has an angle of 14° relative to the sample surface. Since a beam deflection setup is used for the AFM signal, interference with the existing laser and photodiode needs to be avoided. An additional challenge is that the absolute position of the cantilever changes with each newly loaded cantilever since they are placed by hand on the cantilever holder. Thus, a beam steering system in UHV is needed to be able to align the laser to the cantilever tip each time a new cantilever is loaded.

A stick-slip piezo based movable mirror was built that is compatible with our UHV environment. The shear piezo is a thin ferroelectric ceramic plate with polarization along the axis of the plate. When a voltage is applied perpendicular to the the polarization, e.g.

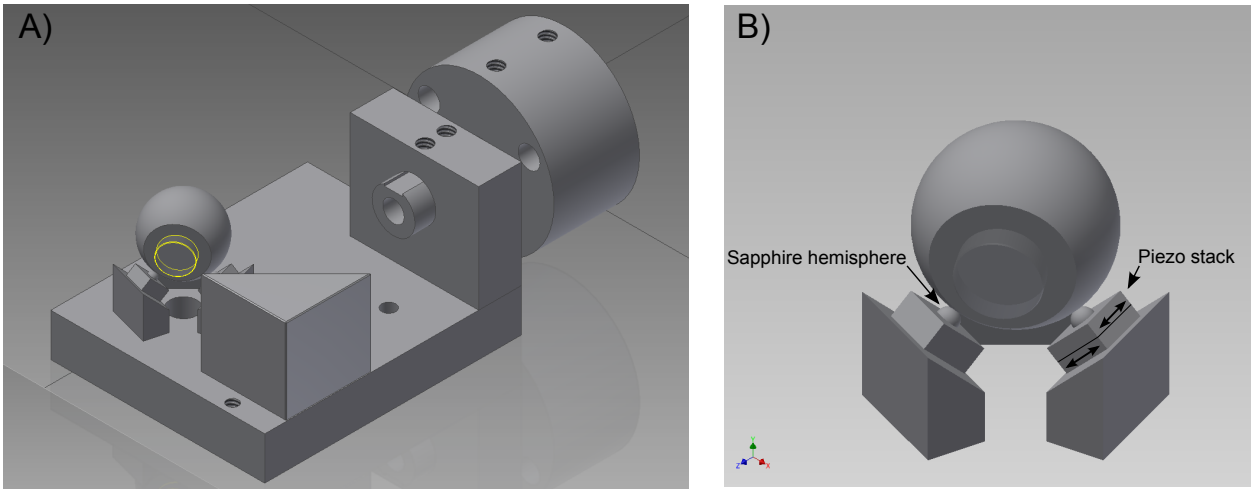

Figure 3.4: A) CAD model of movable mirror assembly. The mirror glued to the sphere is shown in yellow lines. The right angle mirror is used to deflect the incoming beam on the the movable mirror. The beam is entering the UHV chamber trough a window behind the rod seen on the right side. B) close up of the movable mirror. The stainless steel sphere is resting on three sapphire hemispheres. Each hemisphere, is glued to a piezo stack consisting of two piezos oriented 90° to each other.

between top and bottom, a deformation of the material along the polarization occurs [55]. The shear piezo is glued on one side to a holder, while the other side is free to move. A load sitting on the freely movable side of the piezo will move with it when the piezo is slowly extended. During sudden movements of the piezo, the load can not follow because of its inertia. To achieve a movement of the load sitting on the piezos, a sawtooth signal is applied. Such piezo-electric stick-slip actuators are used for many positioning purposes in UHV [55]. For our application we used a spherical rotor. A steel sphere of diameter 5/8″ was flattened, and a 7 mm diameter, 2 mm thick protected silver mirror was glued to it. The

sphere sits on three sapphire hemispheres, each of which are glued to a stack of piezos. The slow motion of the piezo will rotate the sphere while the fast movement of the piezo will not affect the sphere rotation (also known as 'stick-slip' motion). Two axes of rotations are used by having two piezos placed at 90°. It is crucial to be able to adjust the force acting on the piezos. To control this, the magnetic sphere is held down by a magnet placed underneath it. The magnet can be moved closed to the sphere to adjust the force. The adjustment of the magnet needs to be done once before installation. A CAD illustration of the movable mirror assembly can be seen in figure 3.4. A picture of the assembled movable mirror is shown in figure 3.5.

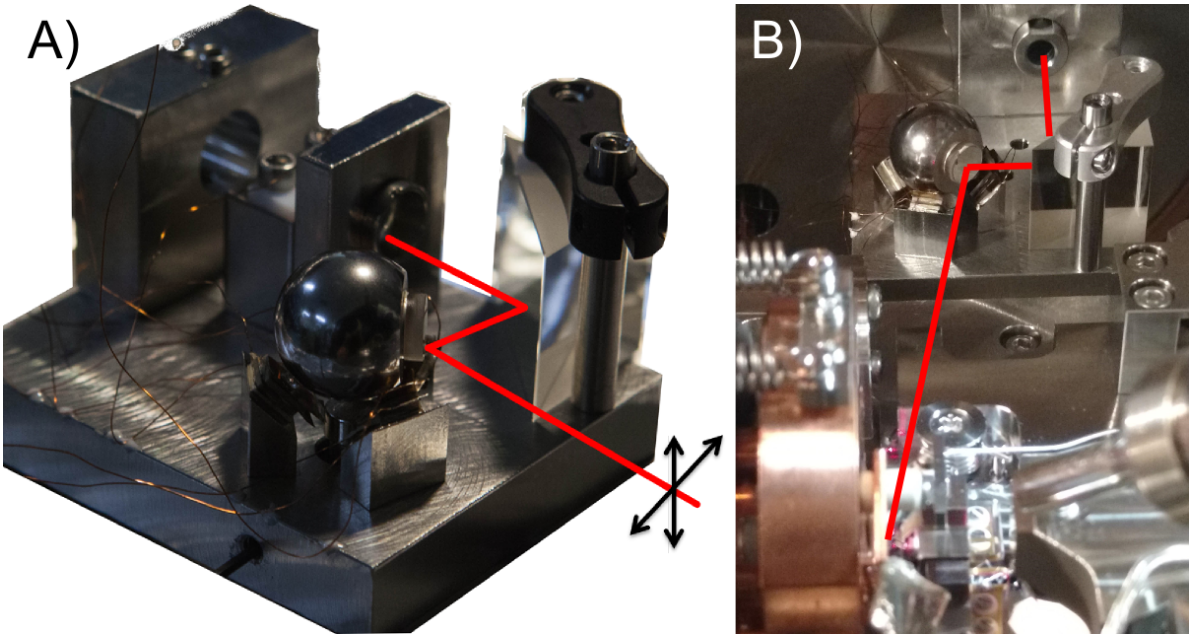

Figure 3.5: A) Picture of the movable mirror assembly before implementation in the UHV chamber. B) The movable mirror inside the UHV chamber. A red line is drawn to illustrate the light path.

3.4 Control System for Piezo Movement

To actuate the piezo, a high voltage sawtooth signal needs to be applied. A Raspberry Pi computer is used to output this sawtooth signal on the audio port. The audio files are pre-generated for easier implementation. The frequency of the sawtooth signal needs to be adjusted to the finished piezo motor for optimal performance. Usually, frequencies between 1-3 kHz are used. The audio signal is amplified with a high voltage (HV) amplifier with a fixed gain of 25. The voltage of the signal feed to the high voltage amplifier can be adjusted to control the amplified voltage. The amplitude might need to be adjusted for each direction of operation. To control the speed of the sphere movement, the number of applied sawtooth cycles are controlled. To control the direction and speed, a Wii remote controller is used that is connected to the Raspberry Pi. A relay switches the high voltage signal between the axis of operation. This allows for the use of one source and one HV amplifier for all signals.

To align the laser to the sample, the movement of the sphere and position of the laser beam are observed with a camera during the initial coarse alignment. A sawtooth signal with more repetitions is used to implement larger movements. For the fine alignment the cantilever deflection signal is monitored until a laser heating effect can be observed, e.g. a change in frequency shift of the cantilever. Once such an effect is observed the beam is moved closer to the sample until the signal vanishes, to guarantee illumination of the sample

without crosstalk effects from the heating of the cantilever. For the fine alignment only a small number of pulses are used per step to achieve a small step size.

3.4.1 Optical Bandpass Filter for AFM Photodiode

Even though the laser is not directly reflected on the photodiode of the AFM system, stray light still reaches the photodiode. Reflections of the modulated light illumination generate a significant signal on the four-quadrant photo diode. Since the expected signal from the AFM modulation is at the same frequency as the light modulation, an optical bandpass filter is installed in front of the beam deflection sensing photodetector. A bandpass filter (Chroma Technology Corp, NC611498, ET670/30nm) is placed in front of the four quadrant photodiode to filter all light coming from the illumination laser, but passes the readout laser from the beam deflection system. A clean signal is acquired after installing the bandpass filter. This filter has the added advantage of minimizing interference with stray light entering the UHV chamber under normal working condition when no laser illumination is used.

4

KPFM of Molecules on Bulk Insulating Substrates

In the following chapter, we will present AFM and KPFM data of pentacene deposited on cleaved potassium bromide (KBr). All data is recorded at room temperature under ultra high vacuum condition ($<6 \times 10^{-10}$ mbar). Pentacene is a widely studied organic molecule. It consists of five benzene rings and classifies as an organic semiconductor. Pentacene was also the first molecule on which submolecular resolution was achieved with AFM [56]. In this study, the electronic properties measured by KPFM will be correlated to illumination with visible light. Therefore, the adsorption of pentacene on an insulating substrate was studied first. KBr was used as a substrate to reduce the interaction of the molecule to the substrate, compared to metal substrates.

4.1 Adsoption on Alkali Halides

Recently, Neff et al. presented a study on the growth of pentacene on alkali halide surfaces observed with AFM and KPFM [42]. Interestingly, mainly two different orientations of pentacene on KBr were found when deposited with a submonolayer coverage. The first is an upright phase, where the height of the layer (16.5 ± 1 Å) corresponds to the expected length of the five carbon rings. The second phase appears much shorter in height (4.5 ± 0.5 Å). The authors concluded that in this phase the long axis of the pentacene molecule must be oriented parallel to the surface of KBr, while the molecule is slightly tilted. KPFM data revealed a difference in CPD for these two types of pentacene islands on KBr. Figure 4.1 shows a sketch of the adsorbed pentacene on KBr as found by Neff et al. [42].

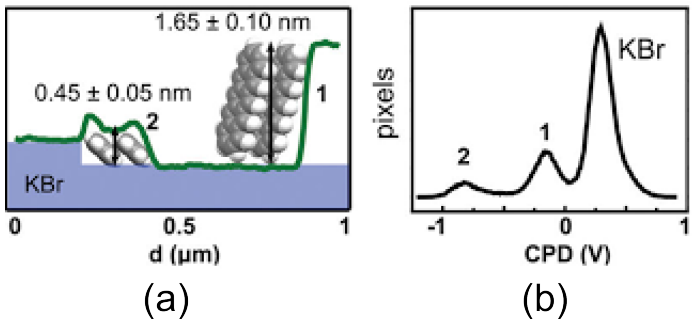

Figure 4.1: (a) Orientation of pentacene adsorbed on KBr is sketched. (b) shows a histrogram of CPD values measured by KPFM. The two types of islands can be destinguished by CPD. Figure adapted with permission from Neff et al. 2014, ACS Nano, [42]. Copyright 2016 American Chemical Society.

KBr is cleaved in vacuum followed by an annealing step at $\sim 150°C$ for four hours to dissipate any residual charges from the cleaving process [57]. Pentacene is thermally evaporated at $145 - 155°C$ for 6 to 7 min to reach a submonolayer coverage in the order of 0.4 monolayer. The rate is calibrated with a quartz crystal microbalance before evaporation. When a stable rate is reached, the microbalance is retracted and the sample is exposed to the evaporator for a specified time to reach the desired layer thickness, based on the measured rate.

Submonolayer coverage of pentacene and an interesting example of pentacene dewetting on KBr can be seen in figure 4.2. Each image has an acquisition time of 42.6 minutes. After evaporation, a small island of pentacene is found and appears with a height of 7.4 Å. The height is calibrated by measuring the step edge of the KBr substrate, giving a height of 3.4 Å with CPD compensation. The measured height of the pentacene island corresponds to the width of a pentacene molecule [58]. This indicates an alignment of the long axis of pentacene parallel to the surface. The $\pi - \pi$ stacking between individual pentacene molecules makes such an alignment favorable. The pentacene island is clearly visible in the KPFM image and can be distinguished from the KBr substrate. Even the step edges of the KBr substrate are visible in KPFM, which is expected due to the different potential at the step edge [40, 41].

While the first and second image shows a pentacene monolayer island, a second layer

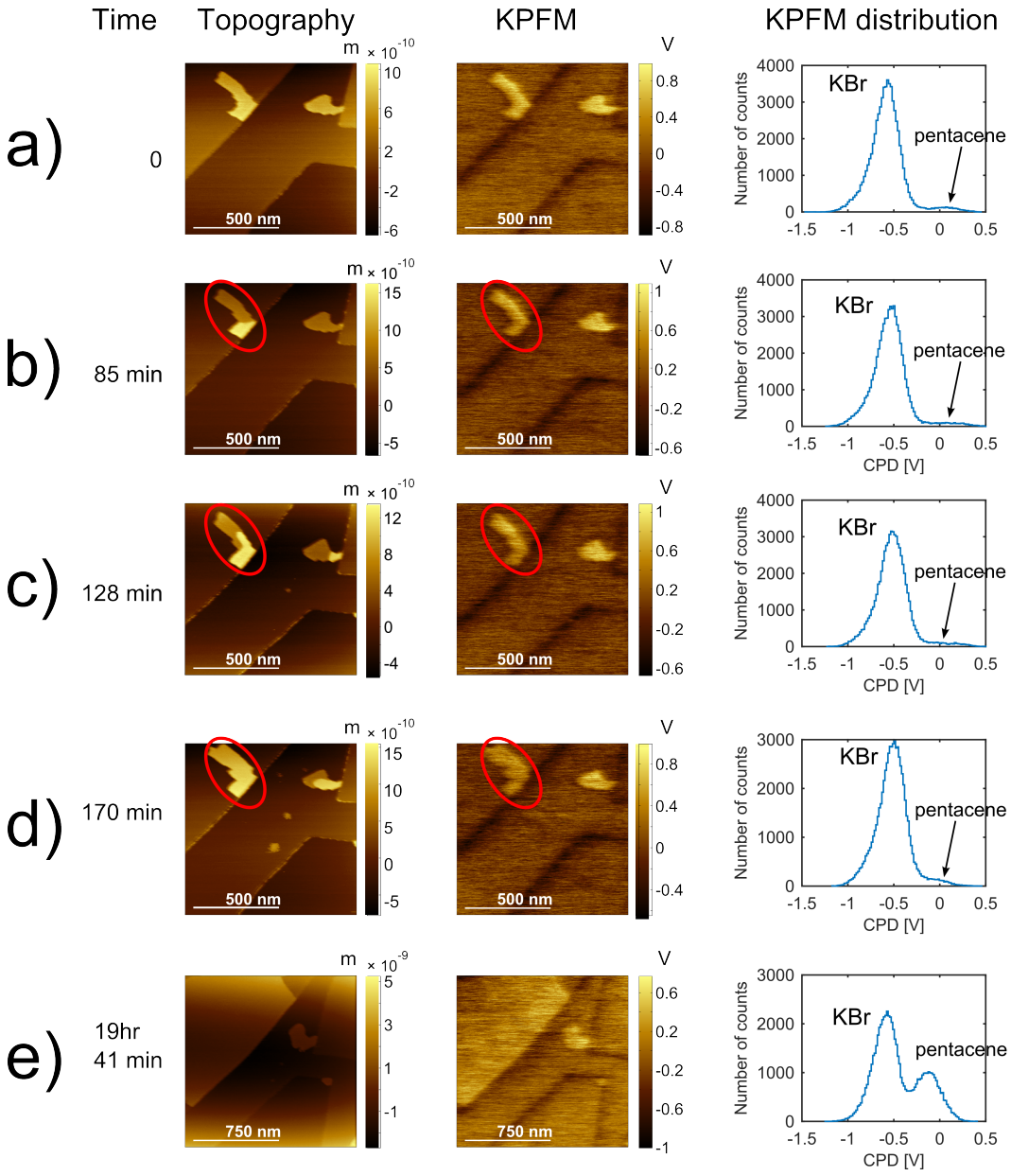

Figure 4.2: Growth of a pentacene island on KBr. First, a monolayer island is observed (a), then the growth of a second layer is visible (b-d in red circle). Further growth of the island is noticed after 19 hours (e). The pentacene island is clearly visible in the KPFM image. The histogram shows the CPD distribution from the KPFM image. Topography images include a plane subtraction.

starts to grow in figure 4.2 b) (after 85 minutes). The second layer slowly grows between image b) and c) and is fully developed in image d) after 170 minutes. The height of the pentacene island is now measured as 14.3 Å. This height is slightly less than the c-axis measured by Nabok et al. of 15.6 Å. Hence, it could be confused with an tilted upright orientation of the pentacene if the growth of the second layer is not witnessed. Molecular dewetting of organic molecules on insulators has been extensivly studied and can be found in many systems [59].

The distribution of the simultaneous acquired KPFM images are shown in a histogram next to each image. The KBr CPD peak is dominating the distribution until the large island appears in image e). The smaller pentacene islands are visible as a small peak. The histogram can be fitted with a gaussian distribution. The large double layer island is found at -140 ± 7 mV.

4.2 KPFM of Pentacene on KBr under Illumination

As previously outlined, the surface photovoltage, which is the change in CPD under illumination, can be measured with KPFM. Here, the surface photovoltage is measured by subtracting two KPFM images. Since KPFM is a relative measurement between the tip and the sample, any changes in the measured CPD could originate from the tip or the sample. Any changes in the tip potential between these images will be visible in the surface photo-

voltage signal. Therefore, the KBr substrate was used as a reference measurement. The KBr potential should not change due to the illumination, since it is not photoactive. Hence, if there is a visible change in the measured CPD of KBr, it must be attributed to a tip change. In order to analyse the KPFM images, the histogram of the measured CPD values is plotted. KBr and pentacene appear as two distinct peaks, as shown in figure 4.2. Figure 4.3 shows four histograms of the same sample area measured in dark, under illumination and followed by an additional measurement in dark conditions after the illumination. Since the KBr potential is used as a reference measurement, all distributions are normalized to the maximum of the KBr peak (set to zero). The change under illumination can be observed between the initial dark measurement and the illumination measurement for the pentacene CPD peak in the histogram (appears above 0.5V). This change under illumination would normally be reported as the surface photovoltage. However, a measurement of the same area under dark conditions(i.e. after the illumination is turned off), does not show the same distribution as before. It does however, show a distribution that is similar to the measurements under illumination. Even a later measurement under dark conditions shows the same CPD. Such a permanent change of the CPD due to illumination under UHV condition is not expected.

To further investigate this behavior, more statistics on the CPD distribution of our sample was acquired. 41 KPFM images were recorded on the same location over 13 hours and 45 minutes. Each image took 25 minutes to acquire. As a reference, two images were

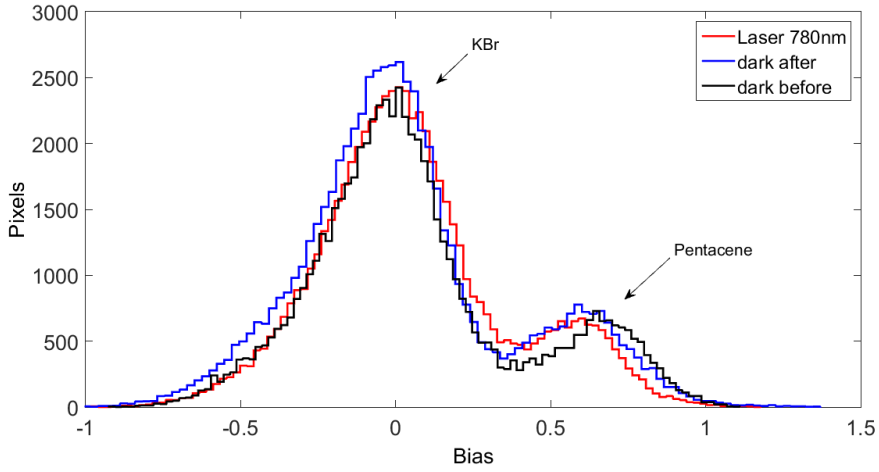

Figure 4.3: Histogram of the normalized CPD measured of pentacene on KBr. The pentacene distribution appears above 0.5 V. Black shows the distribution before light illumination, red during illumination and blue after the illumination.

taken in the dark at the beginning. Then, four different wavelengths were used to illuminate the sample (620 nm, 580 nm, 540 nm and 500 nm). After each change of wavelength, the z-drift of the piezo was monitored until stable conditions were reached. For each wavelength at least two images were taken. After the illumination was turned off and the system cooled down, 30 consecutive images were record overnight under dark conditions. Figure 4.4 shows all 41 histograms of the KPFM images. The histograms are normalized to the CPD of the KBr peak. All images taken under illumination are shown in blue, wheras the dark reference measurements (before and after) are shown in red. The same effect as shown in figure 4.3 can be seen. The distribution of the pentacene peaks under dark illumination is spread over

the same range as the peaks under illumination.

If 9 KPFM images taken with illumination can not be distinguished from 42 KPFM images that were taken without illumination (before and after), no conclusive statement can be made about the change under illumination, yet alone a difference between the used illumination wavelengths. Reliably determining the CPD and thus the surface photovoltage becomes impossible using this sequential subtraction process described and commonly used in the field. This broad CPD distribution is a major concern for our experiment, since we want to observe small changes which are in the same order of magnitude as the distribution observed under dark conditions.

There are various possibilities for the origin of this variance in measured CPD values. The CPD is a relative measurement between the tip and sample and changes in the tip potential will effect the measured CPD. Such changes in tip potential can be due to adsorption of rest gas atoms on the tip. It is known that even under UHV conditions, tip contamination by adsorption of rest gas atoms can occur in less than a minute [60]. This will lead to a broader distribution of CPD values, due to constant rest gas adsorption. However, not only rest gas can effect the tip potential, but also any structural reconfiguration of the tip. Hence, if the tip potential is not the same for the measurement under dark condition and under illumination, the surface photovoltage will change. There is no possibility to distinguish such unwanted changes from the actual surface photovoltage values.

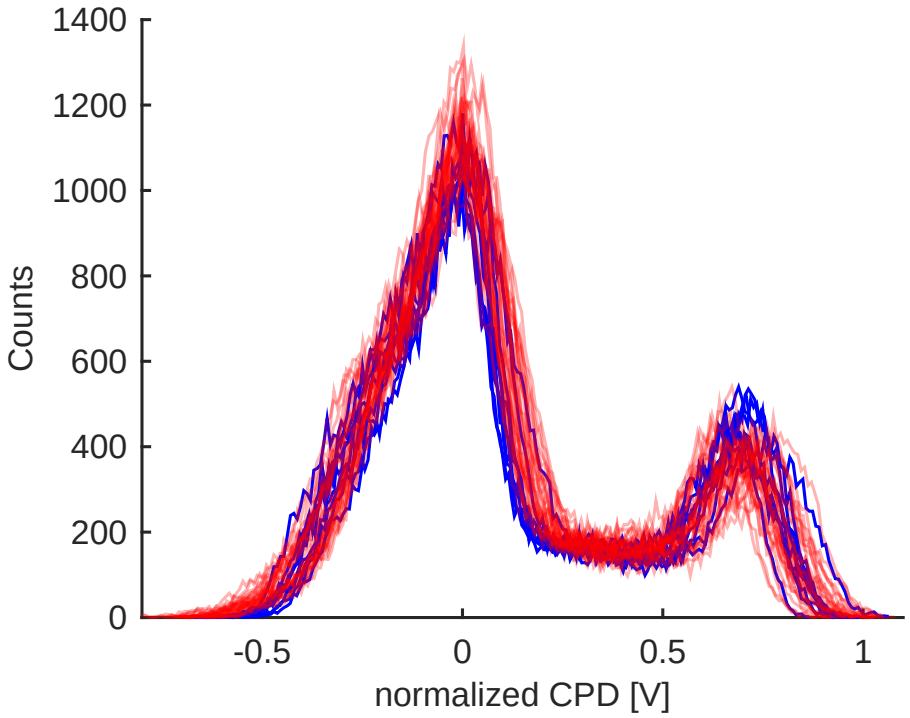

Figure 4.4: Histogram of CPD measured of pentacene on KBr. Red shows the distribution in dark (before and after), blue during illumination.

An additional source for the broad distribution could be pentacene diffusing on the KBr surface as it is not yet confined to an island. As shown in figure 4.2, pentacene is dewetting on KBr. This island growth requires free pentacene diffusing along the substrate. Such a diffusive layer of pentacene would influence the measured CPD.

It has been shown that it is impossible to distinguish the changes in CPD under dark and illumination, as these values change over time. Therefore, a new method for measuring the surface photovoltage is needed. In the next chapter, we will introduce an a novel mea-

surement method to obtain the surface photovoltage under pulsed illumination with AFM. A time-domain analysis of the signal is used and the theoretical background for this is outlined. To illustrate the effectiveness of our new method, surface photovoltage measurements of silicon will be presented and compared between the currently used KPFM approach and our newly developed KPFM method.

5

Measurement of Surface Photovoltage by Atomic Force Microscopy under Pulsed Illumination

This chapter is based on

Measurement of Surface Photovoltage by Atomic Force Microscopy under Pulsed Illumination, Zeno Schumacher, Yoichi Miyahara, Andreas Spielhofer, and Peter Grutter, *Phys. Rev. Applied*, **5**, 044018, **2016**

Abstract

Measuring the structure-function relation in photovoltaic materials has been a major drive for atomic force microscopy (AFM) and Kelvin-probe force microscopy (KPFM). The local surface photovoltage (SPV) is measured as the change in contact potential difference (CPD) between the tip and sample upon illumination. The quantities of interest that one will like to correlate with the structure are the decay times of SPV and/or its wavelength dependence. KPFM depends on the tip and sample potential; therefore, SPV is prone to tip changes, rendering an accurate measurement of SPV challenging. We present a measurement technique which allows us to directly measure the difference in the CPD between illuminated and dark states and, thus, SPV as well as the capacitance derivative by using pulsed illumination. The variation of the measured SPV can be minimized due to the time-domain measurement, allowing accurate measurements of the SPV. The increased accuracy enables the systematic comparison of SPV across different measurement setups and excitation conditions (e.g. wavelength dependence and decay time of SPV).

5.1 Introduction

The structure-function relationship of photoactive materials is of great interest and can be studied with atomic force microscopy (AFM) [9–14]. Two main modes of measurement

can be used: photocurrent and photovoltage measurements. Photoconductive atomic force microscopy (PC AFM) was first presented by Sakaguchi et al. [61] in 1999 using a conductive AFM to measure the photocurrent of organic thin films. Photoconductive AFM was later used by Coffey et al. [62] to map the photocurrent distribution in an organic photovoltaic blend with approximately 20 nm resolution. In 2013, Beinik et al. [63] used PC AFM to investigate the response of ZnO nanorods in a time range greater than seconds.

In contrast to photoconductive AFM, photovoltage measurements can be performed without contact between the sample and the AFM tip. Kelvin-probe force microscopy (KPFM) has become a widely used technique to study not only inorganic but also organic photovoltaic materials [15, 9, 11, 13]. In particular, surface photovoltage (SPV) measurement is commonly used to measure minority-carrier diffusion length [64] and lifetime under illumination in semiconductors [65, 50, 48]. The spatially resolved measurement of carrier lifetime and local recombination rates are of great interest to understand the fundamental charge generation process in photovoltaic materials. SPV values are the result of two measurements typically performed consecutively: $\mathrm{SPV} = \mathrm{CPD}_{\mathrm{illuminated}} - \mathrm{CPD}_{\mathrm{dark}}$ where CPD is the contact potential difference between the AFM tip and sample. The CPD is measured using KPFM in which a dc-bias voltage (KPFM signal) minimizing the electrostatic force is determined with a feedback circuit.

Note that the CPD is the difference between the tip potential and the sample potential-

an intrinsic assumption of CPD measurements using KPFM is, thus, that the tip potential remains constant. This assumption is often violated due to the time it takes to measure the spatial dependence of SPV, its wavelength dependence, or decay times. Note that even under an ultra-high-vacuum condition, tip contamination by adsorption of rest gas atoms can change the tip potential (i.e., the work function) in less than a minute [60]. The accuracy of a SPV measurement is, thus, ultimately limited by the stability of the tip surface potential during the time it takes to measure $\mathrm{CPD}_{\mathrm{illuminated}}$ and $\mathrm{CPD}_{\mathrm{dark}}$. Measurement times can extend over multiple hours or days when the SPV is investigated under various illumination conditions, such as light intensity, wavelength, or polarization, or changes in the sample environment such as the temperature or electric field. Therefore, a measurement method which is insensitive to such tip surface potential changes is needed.

Takihara et al. [66] presented a method to measure the local carrier lifetime with SPV and AFM by using pulsed illumination. By varying the repetition rate of the pulse illumination and measuring the average KPFM signal, a higher time resolution than the KPFM feedback time constant can be achieved. This method has also been used on silicon nanocrystal solar cells [67] and organic photovoltaic materials to study local carrier-recombination rates [15]. Note that the accuracy of the SPV measurement determines the temporal resolution achievable with this approach.

A further limiting factor of conventional SPV measurements based on KPFM is that

they are only sensitive to a change in CPD. However, photocarriers can also contribute to a change in tip-sample capacitance [9]. This change in the capacitance gradient can be measured only if KPFM is performed in bias spectroscopy mode or if the second harmonic signal is measured, which is proportional to the capacitance gradient [68]. As we will show below, a change in the capacitance gradient can lead to a potential systematic error in SPV measurements using established KPFM techniques.

In the following, we present a time-domain KPFM (TD KPFM) approach allowing accurate measurement of the SPV by eliminating the need of a separate reference CPD measurement under dark conditions. TD KPFM takes advantage of pulsed illumination and allows the simultaneous acquisition of full Kelvin-probe force spectra at the same spot under dark and illuminated conditions eliminating the effect of the varying tip potential and capacitance. The change in CPD and capacitance under illumination is measured with TD KPFM.

5.2 KPFM with Pulsed Illumination

KPFM measures the CPD by minimizing the electrostatic interaction between the AFM tip and sample. This is achieved by applying an ac voltage between the tip and sample and minimizing the resulting modulated electrostatic force (F_ω) with a dc bias controlled by a feedback circuit. The applied dc bias yielding a minimum F_ω is equal to the CPD and is independent of the capacitance,

$$F_\omega = \frac{dC}{dz}[V_{dc} - V_{CPD}]V_{ac}\sin(\omega t). \tag{5.1}$$

Under illumination, a change in the capacitance gradient as well as a change in the CPD are expected [9, 11]. Applying a pulsed illumination with the period of T modulates F_ω between two values and can be written as

$$F_\omega = \begin{cases} \frac{dC}{dz}(V_{dc} - V_{CPD})V_{ac}\sin(\omega t), \text{ light off,} \\ \\ \frac{dC^*}{dz}(V_{dc} - V^*_{CPD})V_{ac}\sin(\omega t), \text{ light on,} \end{cases} \tag{5.2}$$

with V^*_{CPD} and dC^*/dz indicating the CPD and capacitance gradient under illumination. Here we assume that the on:off ratio ($T/2$) is unity. As F_ω is measured by a lock-in amplifier, the response time of the feedback τ_{KPFM} is limited by the response time of the lock-in amplifier τ_{loc}.

Since the CPD is now also modulated, we can distinguish between the two cases. When $\tau_{loc} \ll T/2$, the lock-in amplifier can follow the change in CPD, resulting in two distinct values of the KPFM signal that correspond to V_{CPD} and V^*_{CPD}. This condition will, however, limit the pulse rate of the light illumination since the time constant for KPFM feedback is usually fairly slow (greater than a millisecond).

For the case when $\tau_{loc} \gg T/2$, the lock-in amplifier will not be able to react to the change in amplitude in F_ω. Hence, it will not resolve two distinct values of V_{CPD} and V^*_{CPD} but

rather the average of these two values. One might assume this should be the mean of the two CPD values, since the KPFM output is not influenced by the capacitance gradient. However, the output of the lock-in amplifier is a time-averaged value, which can be described by an integration over a full period yielding an averaged F_ω of

$$\begin{aligned}\langle F_\omega \rangle = &\frac{1}{2}\frac{dC}{dz}[V_{dc} - V_{CPD}]V_{ac}, \\ &+\frac{1}{2}\frac{dC^*}{dz}[V_{dc} - V^*_{CPD}]V_{ac}.\end{aligned} \tag{5.3}$$

The KPFM feedback loop will now try to minimize $\langle F_\omega \rangle$ from equation (5.3). It becomes clear that not only the two CPD values but also the capacitance gradient contributes to the average measured value. A change in dC/dz will change the contribution of the two CPD values to the averaged measurement. The minimum of$\langle F_\omega \rangle$ appears at

$$V_{dc} = \frac{dC/dz\ V_{CPD} + dC^*/dz\ V^*_{CPD}}{dC/dz + dC^*/dz}. \tag{5.4}$$

Therefore, V_{dc} of the KPFM output under pulsed illumination is not only sensitive to the change in CPD but also to a change in the capacitance gradient. Hence, the surface photovoltage under pulsed illumination does not solely reflect the change in CPD and can lead to an inaccurate interpretation. Only when there is no change in the capacitance gradient, the KPFM signal will be the average of the two CPD values, $V_{dc} = (V_{CPD} + V^*_{CPD})/2$.

In the following, we present a method based on time-domain spectroscopy that avoids these issues and enables a rapid and accurate measurement of SPV.

5.3 Modulation of Electrostatic Force due to Pulsed Illumination

In contrast to KPFM, which solely measures the CPD, frequency-shift bias spectroscopy (also called Kelvin-probe force spectroscopy, KPFS) can be performed to gain information about the CPD and the second derivative of the capacitance. The frequency shift caused by electrostatic force Δf_e is measured as a function of the applied tip-sample dc bias, resulting in a full Kelvin parabola according to [38]

$$\Delta f_e \propto \frac{dF}{dz} = -\frac{1}{2}\frac{d^2C}{dz^2}(V_{dc} - V_{CPD})^2. \tag{5.5}$$

Fitting equation (5.5) to the experimental data results in the CPD V_{CPD} and the second derivative of the capacitance, d^2C/dz^2. Recall that both the CPD and capacitance gradient change under illumination.

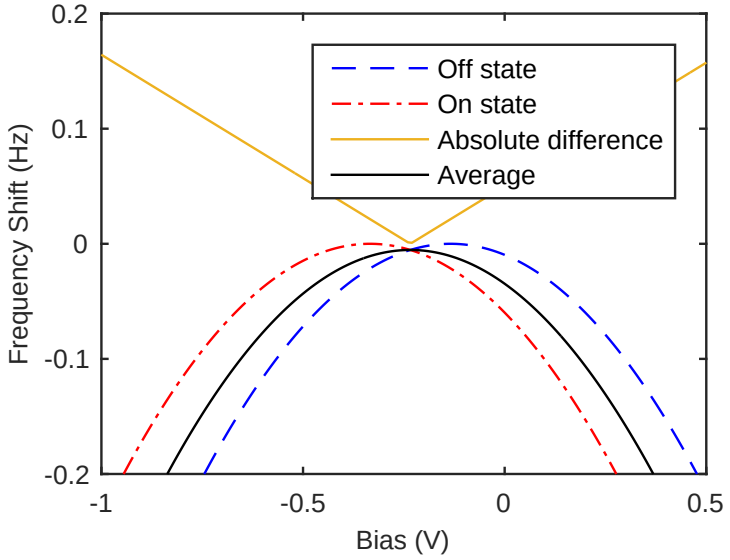

Figure 5.1: Simulated frequency-shift bias spectroscopy for a CDP shift of 200 mV. For illustration purposes, the capacitance gradient is kept constant. A pulsed illumination will modulate the frequency shift at any dc bias between the two curves.

This shift in CPD is illustrated with two KPFS curves in figure 5.1. For simplification, only a shift in CPD (and not the effect of the capacitance gradient) is considered here. As one can see from figure 5.1, for each value of the applied bias a different frequency shift is expected for the two states. A pulsed illumination under a constant dc bias will, therefore, modulate the frequency shift at the rate of the pulsed illumination between the two curves. The modulation frequency can be freely chosen so that the modulation is faster than the time interval between the tip changes but long enough to reach the steady-state value. This modulation effectively implements a sort of common-mode rejection measurement, eliminat-

ing tip (or sample) CPD changes with a longer time constant than the modulation time scale. The detection bandwidth of the frequency detector needs to be higher than the modulation frequency to ensure the measured Δf is following the modulation. The strength of the modulation is equal to the difference in the CPD between the two states. The electrostatically induced frequency shift can be written similarly to equation (5.2) without the V_{ac} modulation,

$$\Delta f_e \propto \begin{cases} \frac{d^2C}{dz^2}(V_{dc} - V_{CPD})^2, & 0 < t < T/2, \\ \frac{d^2C^*}{dz^2}(V_{dc} - V^*_{CPD})^2, & T/2 < t < T. \end{cases} \tag{5.6}$$

The modulation between the two states (Δf_{on} and Δf_{off}) can be measured in the frequency or time domain as described below.

5.3.1 Frequency Domain Measurement

Since the modulation is driven by a square wave (pulsed illumination), Δf is modulated at the frequency of the light illumination (ν) and every odd harmonic. The fundamental harmonic component can be described as

$$\Delta f_\nu = \frac{4}{\pi}(\Delta f_{\text{off}} - \Delta f_{\text{on}}) \sin(\nu t), \tag{5.7}$$

and can be detected by a lock-in amplifier. It becomes clear that the strength of the

modulation at Δf_ν is proportional to the difference in the frequency shift between the two states. A frequency domain measurement can be used to measure the absolute value of the difference (see figure 5.1) between the two states when sweeping the bias (e.g., between the two curves). Such a frequency domain measurement will reject any unwanted tip or sample changes if the modulation frequency is chosen high enough. However, the measurement is still a convolution of the change in the CPD and capacitance gradient.

5.3.2 Time Domain KPFM

The desired signal, the Δf value for both Kelvin parabolas, can be recovered from the Δf channel in the time domain. Instead of measuring the time-averaged signal of the CPD by KPFM, Δf can be integrated over a short time interval after it reaches each steady state, V_{CPD} and V^*_{CPD} in the dark and illuminated state, respectively, as shown in equation (5.8). The integration over a short time in each state yields the two curves corresponding to V_{CPD} and V^*_{CPD}. The integration needs to be performed after the Δf values reach their steady state so that the results are not influenced by the transient values or the delay between the pulses,

$$\begin{aligned} \Delta f_{on} &\propto \frac{1}{b-a} \int_{a}^{b} -\frac{1}{2}\frac{d^2C}{dz^2}(V_{dc} - V_{CPD})^2 \mathrm{d}t, \\ \Delta f_{off} &\propto \frac{1}{b-a} \int_{a+t/2}^{b+t/2} -\frac{1}{2}\frac{d^2C^*}{dz^2}(V_{dc} - V^*_{CPD})^2 \mathrm{d}t. \end{aligned} \tag{5.8}$$

Such an integration of Δf over a short time interval at a defined time within a modulation period can experimentally be realized by a gated integration (see figure 5.2). Within a reference period, the start and duration of the integration can be defined in terms of phase. Here the modulation signal for the pulsed illumination acts as the reference signal. Generally, any modulation (electrical, illumination, thermal, etc.) can be used as a reference signal.

One gated integration interval is set within the illumination-on state, whereas the second integration interval is set within the illumination-off state. This coincides with Δf reaching a maximum or minimum, respectively. A third integrator is set longer than a modulation period to obtain the averaged curve, if desired. The output of each integrator is recorded before the applied bias is changed.

Similar to a regular KPFS measurement, Δf can be integrated at each applied V_{dc} to reconstruct the full Kelvin parabola. In particular, with two different integrations, two curves are acquired, one for V_{CPD} and one for V^*_{CPD}. A schematic of the TD KPFM measurement is shown in figure 5.2.

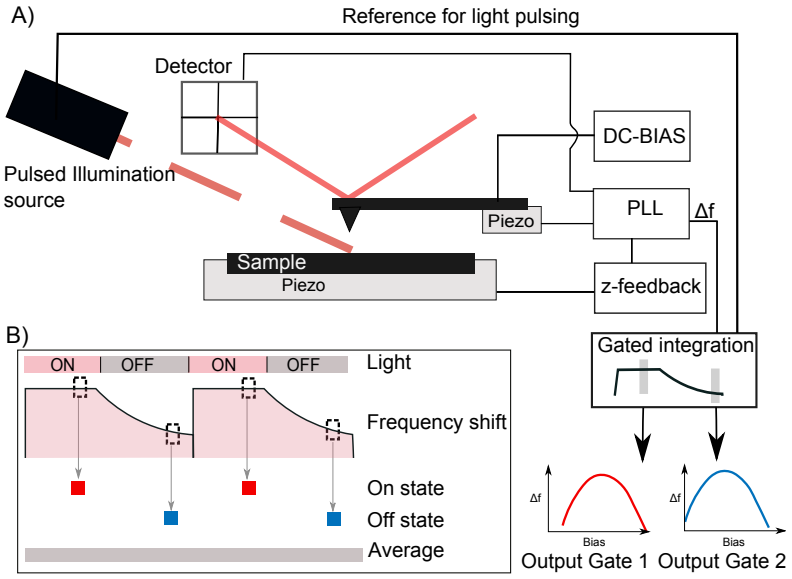

Figure 5.2: A) Block diagram of the TD KPFM measurement. The frequency-shift signal is integrated with two gated integrations synchronized with the pulsed illumination. Each output of the gated integration is recorded at each applied bias to record a full Kelvin parabola. B) Measurement scheme for a gated integration in the time domain of the modulated frequency shift.

5.4 Results and Discussion

As CPD is a relative measurement between a tip and sample, it is possible to measure a photoactive tip. A nonphotoactive sample (cleaved KBr) and a photoactive tip (silicon cantilever) are used to demonstrate an implementation of TD KPFM. The photo absorption in silicon cantilevers under ultra-high-vacuum on a JEOL JSPM-4500A is measured. SPV measurements of silicon were previously reported with metal coated cantilevers [14]. The tip-sample junction is illuminated with a laser at 580 nm, 2.5 mW (FemtoFiber pro TVIS,

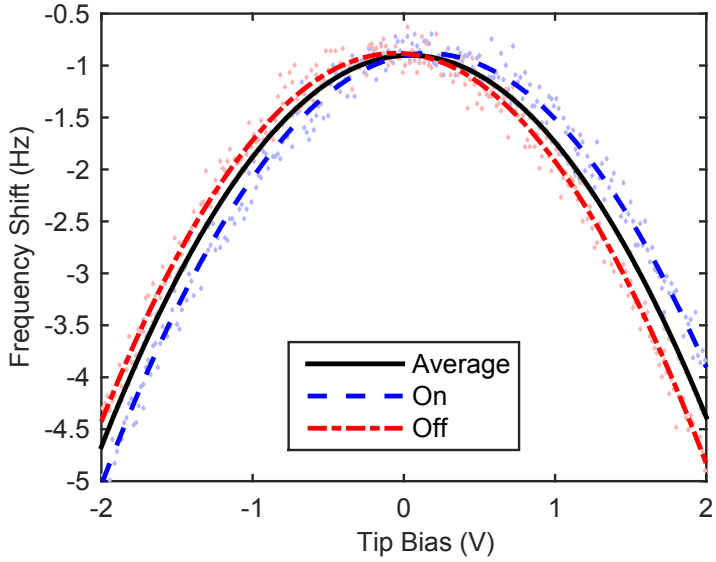

Figure 5.3: TD KPFM measurement of the SPV under pulsed illumination. A gated integration is used to acquire the bias-spectroscopy for the dark and illuminated states simultaneously. A shift of 213 ± 4 mV in CPD and 5% in $\frac{d^2C}{dz^2}$ is measured under illumination.

Toptica), modulated by an optical chopper at 500 Hz. A 50/50 duty cycle is used, resulting in an illumination duration of 1 ms followed by a 1-ms long dark state. The chopper rate is chosen to guarantee the Δf signal reaches its steady state and is not influenced by the time between the pulses. A fast digital lock-in amplifier (UHF, Zurich Instruments) is used as the phase-locked loop (PLL) with a bandwidth of 1 kHz to measure the cantilever frequency. The PLL bandwidth must be set higher than the modulation frequency. The boxcar integration option (UHF-BOX Boxcar Averager, Zurich Instruments) with two gated integrators is used to implement the measurements of Δf_{on} and Δf_{off} [see equation (5.8)]. The starting phase

of each of the two integrators is set so that the signal is integrated around the maximum or minimum of the frequency shift. The output of the two boxcar units is recorded with a Nanonis scan controller. When sweeping the bias, three frequency shift vs bias curves are recorded simultaneously: the two gated integrations containing information about the two different states and the average of the frequency-shift signal. Figure 5.3 shows the measured data and a fitted parabola for each data set. A shift of 213 ± 4 mV in CPD and 5% change in $\frac{d^2C}{dz^2}$ is measured under illumination. This change in $\frac{d^2C}{dz^2}$ is not detected in the SPV measurement using standard KPFM.

To illustrate the robustness of TD KPFM, bias spectroscopy measurements are performed for more than 18 consecutive hours. Figure 5.4 shows a histogram of a simultaneously acquired SPV measurement by TD KPFM and a standard SPV measurement with just one reference measurement at the beginning, repeated 162 times over more than 18 hours. The inset shows two measurements at different times indicated by a and b in the histogram. The average CPD is significantly different between the measurements; however, the difference measured between the on and off state by TD KPFM is not. No spatial drift correction is used during this measurement to test the TD KPDM under the most unfavorable condition. The standard SPV measurement shows a large spread due to a large variability of CPD over time (due to spatial drift as well as tip or sample contact potential changes), whereas the differential TD KPFM measurement is showing a very narrow distribution with a 14-

times smaller standard deviation. The spread in the TD KPFM SPV data originates from a fluctuation of the illumination intensity [50], whereas the KPFM SPV data are also affected by any unwanted slowly varying tip or sample changes. The decreased standard deviation over such a long measurement time is indispensable for studies of changes in the SPV under different illumination conditions (wavelength, intensity, etc.) or sample environment.

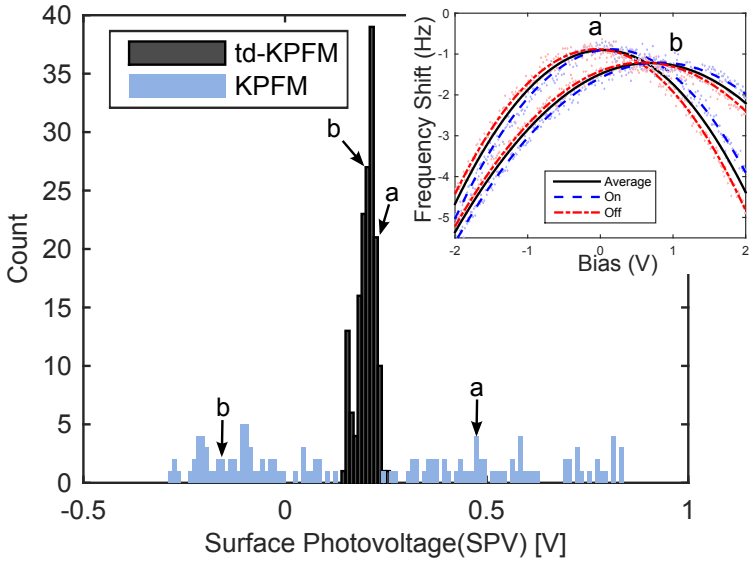

Figure 5.4: Histogram of 162 SPV measurements recorded successively over more than 18 h. The differential TD KPFM SPV measurement (202 mV±22 mV) has a much higher precision than the standard SPV measurement (207 mV±312 mV) with a 14-times-smaller standard deviation. The inset shows two measurements a and b at different times.

5.5 Conclusion

We present a time-domain measurement of a SPV by AFM using a simple-to-implement gated integration method (TD KPFM). This differential TD KPFM measurement of the SPV increases the accuracy by more than an order of magnitude, as it is independent of drift in the tip or sample work function, since it measures only the change in the CPD under modulated illumination. As a demonstration of TD KPFM, we measure the SPV of naturally oxidized silicon over many hours in UHV. Regular KPFM determines a SPV of 207±312 mV, whereas our differential TD KPFM method obtains 202±22 mV, an order of magnitude improvement in accuracy. Achieving this accuracy opens the possibility to compare SPV measurements of the same sample with different tips and even across different laboratories, a crucial step if quantitative theoretical modeling and, thus, physical interpretation of SPV results is to be achieved.

Our analysis of the KPFM theory under pulsed illumination suggests that the output of KPFM is no longer independent of the tip-sample capacitance. Capacitance changes are the result of photon-generated charges in the sample or tip. The technique introduced here, TD KPFM, allows the measurement of true CPD changes under pulsed illumination without the systematic error inherent in standard KPFM due to tip-sample capacitive changes. It is important to note that any measured CPD by KPFM under pulsed illumination is affected

by the change in capacitance in any sample and is not limited to inorganic semiconductors. Hence, it is crucial to quantify the change in capacitance to get the true change in the CPD if pulsed illumination is used. Recently presented minority-carrier lifetime measurements [66, 67, 15] all rely on pulsed illumination. Thus, TD KPFM should be used for such minority-carrier lifetime measurements. By making SPV measurements independent of tip effects, TD KPFM will greatly improve the accuracy and time resolution of carrier lifetime measurement.

We note that this time-domain approach of measuring a modulation in AFM is not limited to SPV and KPFM measurements. It can be extended to any modulation of the tip-sample interaction, such as electric or thermal pulses. Especially for cases with square wave modulation, where lock-in techniques measure only the first Fourier component, this gated time-domain approach can be of great interest. With this gated time-domain approach, the absolute values of the modulated signal (e.g., frequency shift, CPD, etc.) can be recovered rather than just the strength of the modulation (e.g., average CPD, etc.). This is demonstrated with TD KPFM where the CPD and $\frac{d^2C}{dz^2}$ values are recorded instead of the average CPD over the modulation. When such pulses are used to study decay times, the increased accuracy will allow a better determination of the time-dependence reaction of the system to these pulses, e.g., mobility if the potential is pulsed or minority-carrier lifetime if the illumination is pulsed.

6

The Lower Limit for Time Resolution in AFM

Time-resolved measurements with AFM can be of great interest due to the high spatial resolution of AFM. Mapping spatial variations in the time response of a sample allows further insight into the structure-function relationship. In the case of surface photovoltage (SPV) measurements, the time resolution gives information about the lifetime of the photo-excited carriers. Time-resolved SPV by AFM, therefore, measures the local lifetime of photo-excited carriers determined by the spatial resolution of the AFM. Note that measuring the decay time of the electric force in AFM can be of interest in many other AFM applications, such as ion diffusion in battery materials or propagation of electric pulses along nano-materials [69, 70].

Achieving time resolution with AFM measurements is nontrivial because of the bandwidth limitation of the mechanically oscillating cantilever and the involved electronic feedback loops. In non-contact AFM (nc-AFM), the phase locked loop (PLL) measuring the frequency shift of the cantilever response is one of the slower components of the feedback loop. A diagram illustrating the different response times in AFM is shown in figure 6.1. The bandwidth is commonly set between a few tens of Hz to kHz in order to achieve a reasonable signal-to-noise ratio. This allows for the direct observation of a time response in the low millisecond regime. Even with high-frequency cantilevers ($\sim$MHz) and high PLL bandwidth (300kHz), the fastest measurable signal will be in the order of tens of microseconds. Therefore, any processes that occur on a time scale faster than microseconds requires a different approach. To achieve higher scanning speeds or faster time resolution, the common belief for nc-AFM is to increase the modulation frequency, i.e. the mechanical resonance frequency of the cantilever as well as the BW of the PLL. However, the response time of the cantilever will always be the limiting factor for a direct observation of time-dependent effects. Picosecond time resolution would need cantilevers operating at 1 THz. This is not feasible, as 1 THz corresponds to molecular rotation/vibration frequencies.

In 1990, R. Hamers and D. G. Cahill presented a first approach to ultrafast time resolution in scanning capacitance microscopy by pulsed laser illumination [71, 72]. They pointed out that a time resolution faster than the bandwidth of the feedback electronics can be

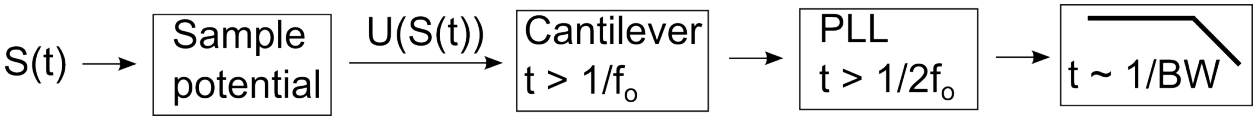

Figure 6.1: Signal flow in AFM. The response time of each element is indicated. The sample potential is stimulated by an external signal $S(t)$. The cantilever reacts to the potential $U(S(t))$ with a minimum response time of one period $(1/f_0)$. The fastest PLL can measure this change in two cycles. A low-pass filter is used to limit the signal to noise ratio.

achieved and is only limited by the time response of the underlying physical process of the sample. The proposed idea uses a modulated signal $S(t)$ to generate a non-linear response in the sample $R(S(t))$. For a linear responding system, the average signal will correspond to the average of the stimulating signal. However, for a non-linear response the average of the response $\langle R(S(t))\rangle$ will depend on the temporal distribution of the stimulating signal, $\langle R(S(t))\rangle \neq R(\langle S(t)\rangle)$.

Conveniently, the SPV decay is a non-linear response. Therefore, for non-linear response experiments measuring the SPV decay, TD KPFM presents a great tool to measure the time-resolved surface photovoltage using pulsed illumination. These experiments follow a pump-probe type of experiment, which is discussed in more detail in the following section.

A pump-probe type of measurement with AFM was reported by Jahng et al. in 2015 on bulk silicon naphtalocyanine (SiNc) [32]. A two beam optical excitation was used to excite the cantilever at the second resonance frequency via the photo-induced dipoles in the tip

and the sample. The amplitude of the second harmonic is recorded while the delay between the two beams is changed, revealing the same ps decay dynamics measured with optical transient absorption measurements. This was an additional proof of the capability of AFM to measure fast signals. However, it is limited to the dipole interaction between the tip and the sample induced by an optical pulse.

In this chapter, we will develop a general understanding of the fastest possible time scale measurement with nc-AFM, independent of the nature of the modulating signal (e.g. electric, thermal, light).

6.1 Measuring non-linear Signal Decays with FM-AFM

In the following, we will describe how to generically measure a non-linear decaying signal with nc-AFM. This general analysis is not limited to a specific response or time constant and can, therefore, be applied to any time scales and any stimulating signal. It will also allow us to understand what determines the ultimate limitations of time resolution measurements by AFM.

In fm-AFM, the frequency shift of the oscillating cantilever is measured. In the small amplitude limit, the frequency shift is proportional to the force gradient between the tip and the sample:

$$\Delta f = -\frac{f_0}{2k}\frac{\partial F_{\mathrm{ts}}}{\partial z} = \frac{f_0}{2k}\frac{d^2 U_{\mathrm{ts}}}{dz^2} \tag{6.1}$$

where k is the spring constant, F_{ts} the force between tip and sample, f_0 the resonance frequency of the cantilever and U_{ts} the tip-sample potential.

For large amplitudes, various methods have been used to find an equivalent solution [35, 34]. In general, the frequency shift is related to the average of the tip-sample force F_{ts} during a full cantilever oscillation [3]:

$$\Delta f = -\frac{f_0}{kA_0^2}\langle F_{ts}\rangle = -\frac{f_0}{kA_0^2}\frac{1}{T_0}\int_0^{T_0} F_{ts}[d + A_0 + A_0\cos(2\pi f_0 t)]A_0\cos(2\pi f_0 t)dt, \qquad (6.2)$$

with d the distance of closest approach and A_0 the cantilever amplitude.

Equation 6.1 and 6.2 do not take any time-dependent tip-sample interactions into account. However, it does tell us that the cantilever acts as a low-pass filter averaging over F_{ts} during one oscillation period. Consequently, one would assume that any changes in F_{ts} faster than T_0 would not be resolvable in the frequency shift. In the following, we will discuss how to overcome this apparent limitation. To have a general discussion, we will first apply our analysis to a generic potential $U(t)$. The interaction of a nc-AFM tip with this potential $U(t)$ will translate to a measurable frequency shift according to equations 6.1 and 6.2.

Following the approach of Hamers and Cahill [71], assume an external signal $S(t)$ is applied to modulate the potential $U(t)$. In nc-AFM, such modulations are often sine waves, e.g. in KPFM, an AC voltage is applied to modulate the electrostatic force. However, we will apply a pulsed signal to modulate the tip-sample potential. The modulation signal can be

of any nature, such as electrical, thermal, optical, etc., as long as it generates a modulation of the potential $U(t)$ which translates to a modulation of the force and force gradient. Note that the concepts developed in the following map on to classical pump-probe experiments using the oscillating cantilever as a mechanical detector similar to a slow photodetector.

In the following we assuming a pulsed modulation with the response exhibiting an exponential decay once the stimulation is over:

$$U(t) = \begin{cases} U_0 & \text{for } 0 < t < T_p, \\ U_0 e^{-t/\tau} & \text{for } T_p < t < T_{rep}, \end{cases} \tag{6.3}$$

with a pulse duration of T_p, a potential amplitude U_0 and a repetition rate of $1/T_{rep}$. This pulse will be referred to as the pump pulse hereafter. We assume a saturation of the response amplitude at U_0, hence both pulses will have the same maximum response.

The decay time τ is the property of interest which we want to measure with AFM, because it gives information about the time scale of the SPV decay. We assume this decay to be faster than the PLL response of our nc-AFM feedback and therefore, it can not be observed in real time. More specifically, we want to focus on the case when the decay and pulse width are shorted than the cantilever oscillation period. A second pulse (probe pulse), at the same repetition rate as the pump pulse, is introduced to generate two pulse trains which can be delayed in time with respect to each other. This principle can be seen in figure 6.2.

Within one cycle T_{rep}, one pump pulse and one probe pulse is present and separated by

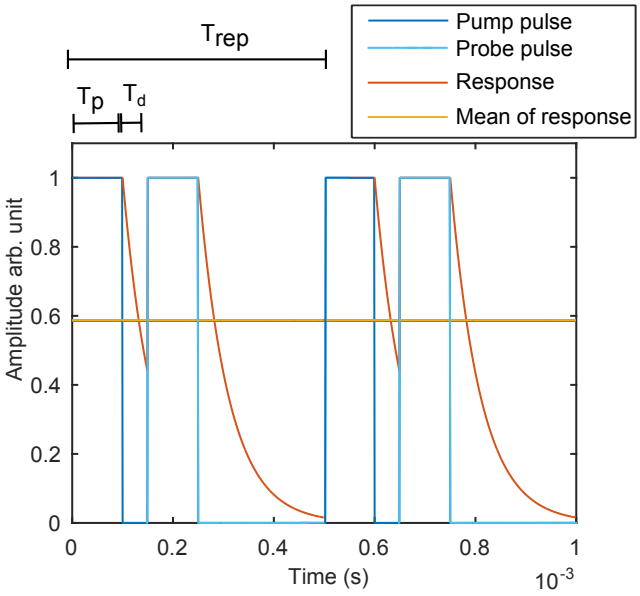

Figure 6.2: Simulation of stimulated pulse train and potential response with an exponential decay. The pump pulse is shown in dark blue and the probe pulse in light blue. The time notation used in equation 6.5 are indicated as T_p as the pulse width, T_d as the delay time and T_{rep} as the inverse of the repetition rate.

the delay time T_d. The potential response can now be expressed as:

$$U(S((t)) = \begin{cases} U_0 & \text{for } 0 < t < T_p, \text{ pump pulse,} \\ U_0\ e^{-t/\tau} & \text{for } T_p < t < T_p + T_d, \text{ decay,} \\ U_0 & \text{for } T_p + T_d < t < 2T_p + T_d, \text{ probe pulse,} \\ U_0\ e^{-t/\tau} & \text{for } 2T_p + T_d < t < T_{rep}, \text{ decay.} \end{cases} \tag{6.4}$$

As shown in equation 6.2, the frequency shift is related to the average of the tip-sample

force F_{ts}, hence to $\partial U(t)/\partial z$. The average of each section in equation 6.4 corresponds to the integral divided by the width of the integral.

$$\langle U(S(t))\rangle = \begin{cases} U_0 & \text{for } 0 < t < T_p, \\ \frac{\tau U_0}{T_d}(1 - e^{-T_d/\tau}) & \text{for } T_p < t < T_p + T_d, \\ U_0 & \text{for } T_p + T_d < t < 2T_p + T_d, \\ \frac{\tau U_0}{Trep - T_d - 2T_p}(1 - e^{-(T_r ep - T_d - 2T_p)/\tau}) & \text{for } 2T_p + T_d < t < T_{rep}. \end{cases} \tag{6.5}$$

During the course of the experiment, the delay time T_d will be varied to delay the pulses relative to each other. The second and fourth term of equation 6.5 will change accordingly. Hence, when the average of the potential as a function of delay time is recorded, the decay constant τ can be recovered, as shown in detail below. It can be concluded that only the contribution of the segment containing the exponentially decaying signal will change when the delay time is varied.

Since the time constant τ can be recovered from the average signal, the cantilever itself can be used as an averaging tool. It is not possible to resolve the individual changes in frequency shift due to the averaging of the cantilever, when the decay of the sample is much faster than the response time of the cantilever. However, the average potential will be different depending on the delay times between the pulses as shown in equation 6.5. The only requirement necessary is that the cantilever is capable of resolving the change in average

potential between two different time delay settings. The lower limit for this is given by the minimal detectable force gradient as described by Albrecht et al. [7].

From equation 6.5, the average potential over one cycle of T_{rep} can be calculated, which will be the same as the average over any multiple of T_{rep}.

$$< U(S(t)) >= \frac{2U_0T_p}{T_{rep}} + \frac{T_d\tau U_0}{T_{rep}T_d}(1 - e^{-T_d/\tau}) + \frac{(T_{rep} - T_d - 2T_p)\tau U_0}{T_{rep}(T_{rep} - T_d - 2T_p)}(1 - e^{-(T_{rep}-T_d-2T_p)/\tau})$$
$$= \frac{2U_0T_p}{T_{rep}} + \frac{\tau U_0}{T_{rep}}(2 - e^{-T_d/\tau} - e^{-(T_{rep}-T_d-2T_p)/\tau}) \quad (6.6)$$

The average response needs to be measured at different delay times T_d, to recover the decay time from the averaged measurement. The average potential from equation 6.6 includes additional terms besides the decay time. The first term is dependent on the potential response U_0. As shown in chapter 4, the tip-sample potential can change over time due to drift in the CPD. To ensure the decay time is accurately measured and not distorted by a drift in the system, a modulation of one of the two pulse trains can be used for a differential measurement. By measuring the difference between the train on/off condition, the effect of the delay pulses is measured and any drift in the system is nulled. This modulation of the pulse train will produce a modulation of the frequency shift of the cantilever at the frequency of the modulation.

The stimulating signal now consists of a sequence of two pulse trains, delayed with respect to each other (i.e a pump and a probe pulse), of which one is modulated at a

low frequency. This is equivalent to a pump-probe experiment, with a continuous pulse train (pump pulse) and a modulated pulse train (probe pulse). Instead of measuring the optical properties of the probe pulse the tip-sample potential is measured. This allows for a reference measurement between states with and without delayed probe pulses, similar to the TD KPFM measurement previously presented. The measurement scheme is shown in figure 6.3.

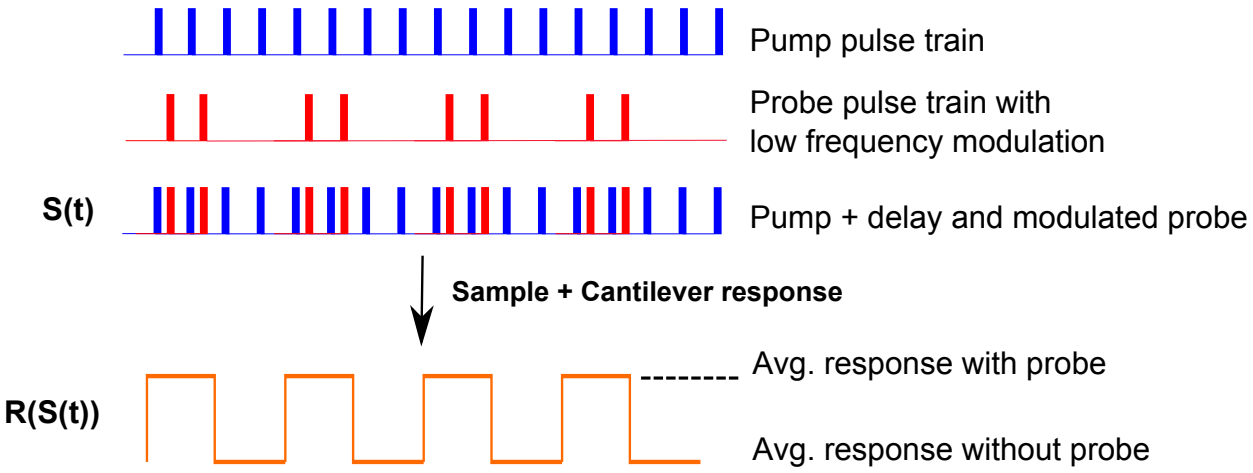

Figure 6.3: A pump pulse train (blue) and a probe pulse train (red) are delayed with respect to each other. The probe pulse train is additionally modulated. The final pulse train pattern consists of the delay pulse trains with and without the probe beam present. The sample and cantilever react to this pulse train resulting in two states.

The average potential with just one pulse train, which is used as the baseline, can be calculated as,

$$< U_{baseline}(S(t)) >= \frac{U_0 T_p}{T_{rep}} + \frac{\tau U_0}{T_{rep}}(1 - e^{-(T_{rep}-T_p)/\tau}). \tag{6.7}$$

This gives the ability to use a baseline subtraction. The difference between the average probe pulse on/off is

$$< U(S(t)) >= \frac{U_0 T_p}{T_{rep}} + \frac{\tau U_0}{T_{rep}}(1 - e^{-T_d/\tau} - e^{-(T_{rep}-T_d-2T_p)/\tau} + e^{-(T_{rep}-T_p)/\tau}). \tag{6.8}$$

The first and last term of the sum are constant. Only the third and fourth term will contribute to a change in the average when T_d is modulated. Therefore, the time resolution is solely coming from:

$$< U(S(t)) >= \frac{\tau U_0}{T_{rep}}(1 - e^{-T_d/\tau} - e^{-(T_{rep}-T_d-2T_p)/\tau}). \tag{6.9}$$

A suitable designed experiment will allow the last term in equation 6.9 to be neglected by implementing a repetition time T_{rep} that is much larger than the pulse width and the delay. This expression now allows us to determine the minimum measurable time constant τ by AFM in terms of an energy problem. Therefore, it is no longer a question of how fast the measurement can be done, but rather how small of a potential energy change can be measured. To determine this, there is a well-known expression of the thermal limit of AFM. Hence, the minimal change in potential energy due to the non linear decay found in equation 6.9 needs to be equal to the minimum measurable energy in AFM [73]:

$$\frac{\tau U_0}{T_{rep}}(1 - e^{-T_d/\tau}) = \frac{2k_B T}{\pi \omega_0 Q \tau_s} \tag{6.10}$$

where τ_s is the integration time (proportional to the inverse of the bandwidth, see figure 6.1) used in the experiment. We can see from equation 6.10 that our average potential increases with higher repetition rate (e.g. time between pulse pairs). This is expected since the system is pumped more often. As expected, it also depends on the initial response amplitude U_0. Thus, having a large response to the simulating signal is obviously beneficial. The faster the signal decays (small τ), the smaller the averaged potential change measured. The difference in potential between a step in T_d is given by the ratio of T_d/τ. Note that a ten times smaller T_d than τ will result in an approximately 10 % decrease of $\tau U_0/T_{rep}$. Assuming $T_d \ll \tau$, the minimum decay time constant is equal to:

$$\tau = \frac{T_{rep}}{U_0(1 - e^{-\beta)}} \frac{2k_B T}{\pi \omega_0 Q \tau_s} \tag{6.11}$$

with $\beta = T_d/\tau$, e.g. the ratio between the delay time and the decay time constant.

6.1.1 Calculation of Frequency Shift Response

A simple numerical calculation of the integral in equation 6.2 can give the expected frequency shift response due to two delay pulse trains. For two pulse trains in the form of equation 6.4, the integral is numerically calculated for one oscillation period of the cantilever. The time is

given in units of T_0. The pulse train has a repetition rate of $\frac{1}{256}\ T_0$ and a pulse duration of $\frac{1}{256*64}\ T_0$. Hence, there are 256 pulses during one cantilever oscillation. A fast decay constant of $0.02*\frac{1}{256}\ T_0$ was chosen. For each delay setting, the integral of $F_{ts}cos(2\pi t)^2$ was calculated. A plot of this calculation versus delay time is shown in figure 6.4. The numerically calculated data was fitted to the analytical solution from equation 6.8. The time constant obtained from the fit ($7.8125 \times 10^{-5} \pm 2 \times 10^{-9}\ T_0$.) agrees within errors with the time constant used in the numerical calculation ($7.8125 \times 10^{-5}\ T_0$). This simple calculation illustrates that much shorter pulses compared to the cantilever oscillation will have an effect on the frequency shift, if they are delayed with respect to each other.

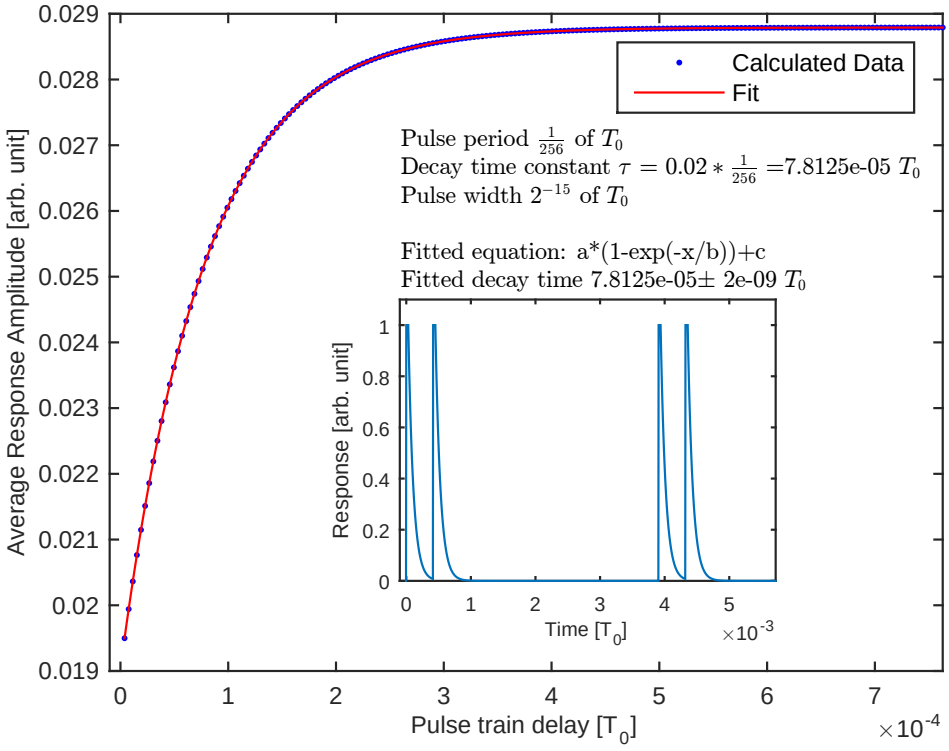

Figure 6.4: Numerical calculation of the integration in equation 6.2 for a F_{ts} in the form of equation 6.4. The data was fitted to an exponential decay, according to equation 6.8. Note that the time is given in units of the cantilever oscillation (T_0). A pulse period of 2^{-8} T_0 and pulse width of 2^{-15} T_0 is used. The inset shows the pulse shape and exponential decay for one delay setting. A decay of 7.8125×10^{-5} T_0 was used for the model. An exponential fit results in a decay of $7.8125 \times 10^{-5} \pm 2 \times 10^{-9}$ T_0.

6.2 Experimental Implementation

The proposed modulation scheme shown in figure 6.5 is generic and can be implemented with an arbitrary pump signal. Any stimulating signal leading to a non-linear interaction, which can be applied as a pulse train, can be used. To determine ultrafast decay times, two pulse trains are needed that can be delayed in time with respect to each other. For our application of measuring the photo-carrier decay, the stimulating signal is a ultrafast pulsed laser source. Ultrafast laser sources can produce laser pulses with a pulse width below 100 fs. A delay between two pulse trains can easily be generated with an optical delay stage. Such a setup is sketched in figure 6.5.

To measure the average potential generated by the delayed pulse trains, a modulation of the pump pulse is used which translates into a modulation of the frequency shift. Here, the modulation of the frequency shift is measured with either a gated integration setup or a direct sideband lock-in detection. As outlined in the previous chapter, a modulation of the probe beam will enable an accurate, drift free measurement of the tip-sample potential and thus allows the measurement of the non-linear decay. The same modulation principle was previously used in TD KPFM to avoid any drift for measurements of longer duration [74].

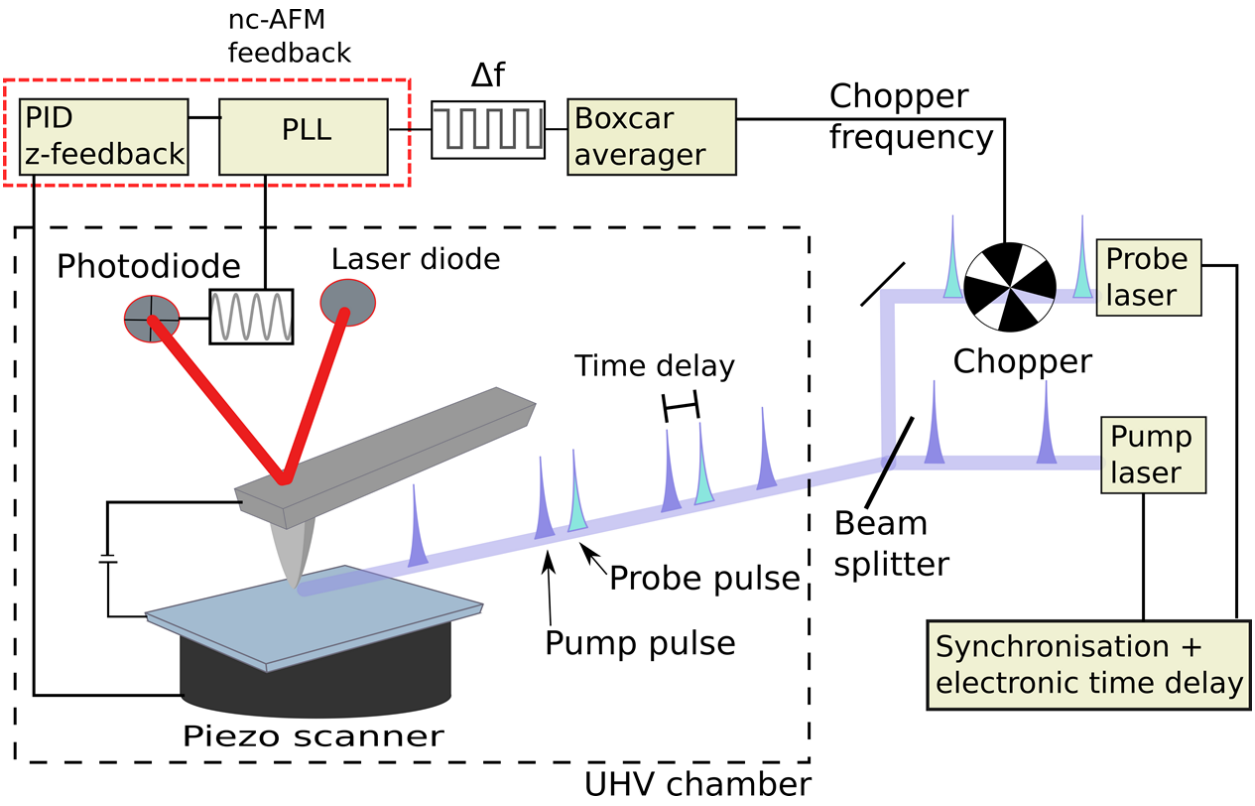

Figure 6.5: Two pulsed light sources are combined (pump and probe). The probe beam is modulated with an optical chopper to generate a baseline response. The delay between the two pulse trains is controlled electronically. The modulation of the frequency shift signal is recored with a boxcar averager.

It is important to note that the modulation of the probe beam needs to be slow enough to be resolved by the PLL. Otherwise, the measured signal will either be influenced by the PLL dynamics, or not reach the steady state signal after the pulsed illumination. The frequency shift can then be integrated over a short time interval when no transient effects from the

PLL are present. Having a boxcar integration with baseline subtraction allows for the direct measurement of the probe beam effect (see equation 6.8). This difference will decay with τ while the delay between the two pulse trains is swept across the range of interest.

A lock-in measurement at the probe pulse modulation frequency gives information about the difference between the two states, hence the decay times. For imaging purposes, such a measurement might be well suited. However, if more information needs to be extracted from the change in signal, such as the change in capacitance gradient shown by TD KPFM, only a gated integration in the time domain will provide this additional information.

6.3 Ultrafast Decay in Low Temperature Grown GaAs

The photocarrier decay in low temperature grown GaAs (LT-GaAs) is an ideal sample to verify the above suggested measurement of ultrafast time scales in AFM. LT-GaAs has a carrier lifetime in the low picosecond regime, depending on the growth conditions [75]. During the growth process many point defects are created [76, 77]. These defects lead to a short diffusion length of the injected charge carrier and hence a short life time. For our measurement, we used a LT-GaAs sample from TeTechS (TeTechS Inc., Ontario, Canada) with a carrier lifetime of about 1 ps. A 1.5 μm lt-GaAs layer was grown on a 200nm AlAs etch stop layer. The substrate consists of approx. 600 μm thick semi-insulating GaAs. The LT-GaAs layer is thicker than the penetration depth of the used illumination and therefore no

contribution of the substrate is expected. The penetration depth was calculated to be 653nm for an illumination with 780nm and 253nm for illumination with a 610nm wavelength[78]. Our UHV AFM setup was used in combination with our ultrafast pumped laser source (described in section 2). The 780nm laser (Toptica FemtoFiber Pro NIR,80.1 MHz, 94 fs pulse width) is used with a power of 29.8 mW (0.182 nJ/cm^2) and the TVIS (Toptica FemtoFiber Pro TVIS, 80.1 MHz, 0.4 ps) is adjusted to a 610 nm wavelength with an average power of 5.125 mW (0.032 nJ/cm^2). The fluence is low enough to avoid extensive heating of the AFM tip[79]. The 610 nm beam is chopped at a low frequency (233 Hz) to generate a frequency modulation shift. Both lasers are locked to the same repetition rate with the variable repetition rate (VAR) and Laser repetition rate control (LRC) option from Toptica included in the NIR FemtoFiber Pro. An electronic delay between the lasers can be adjusted by adding a phase offset to the phase lock. This electronic delay was used to delay the two laser pulses relative to each other. The rms-jitter of the two locked lasers is measured to be 130 fs.

A UHF lock-in amplifier from Zurich Instruments with the boxcar averaging option is used for data acquisition. All sideband lock-in measurements are performed with a HF2PLL from Zurich Instruments with a direct sideband detection.

To verify the change in CPD under pulsed illumination, the LT-GaAs sample is illuminated with 780 nm and TD KPFM is used to measure the surface photovoltage under pulsed

illumination. A surface photovoltage of 96 ± 8 mV is measured for this sample (see figure 6.6).

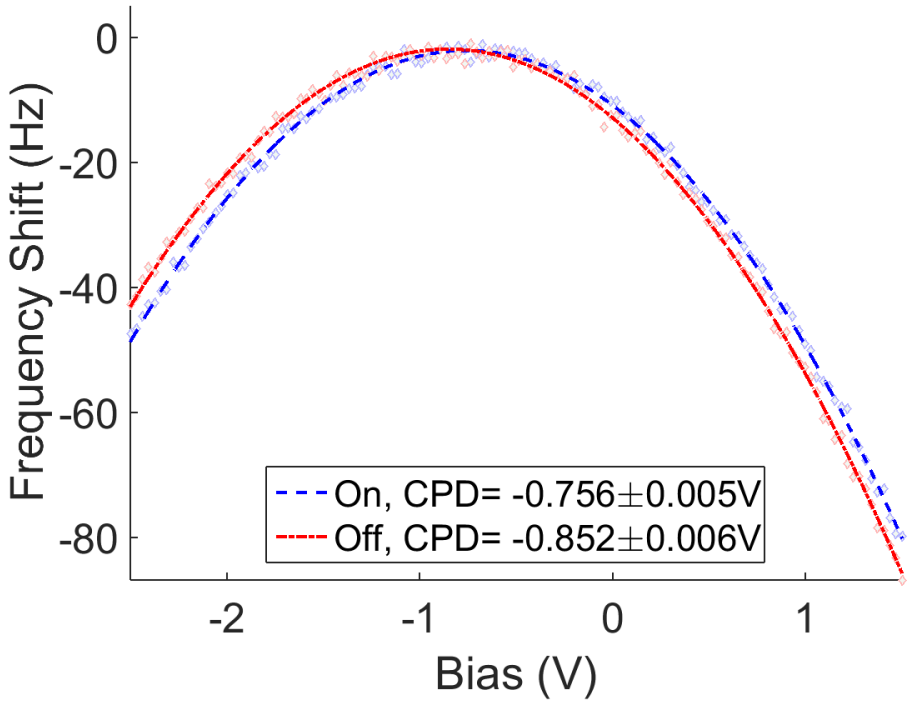

Figure 6.6: Surface photovoltage of LT-GaAs measured with TD KPFM. A surface photovoltage of 96 ± 8mV is measured between the on (blue) and off (red) Kelvin parabola.

The recorded change in frequency shift as a function of the delay time between the two laser pulses is plotted in figure 6.7. The direct sideband detection (figure 6.7a) is performed simultaneously with the boxcar averaging (figure 6.7b). The data was fitted with a simple exponential decay since a low fluence is used [80, 76]. A decay time of $\tau = 1.1 \pm 0.4$ ps for the sideband detection and $\tau = 0.9 \pm 0.6$ ps for the time domain boxcar averaging is

measured by fitting an exponential decay in the form of $a(1 - exp(-x/\tau)) + c$. This lifetime is in the expected range of 1 ps within error for both measurements. The fitting term c corresponds to the value at zero delay, hence the first term from equation 6.8. The term a is equal to the increase in signal between zero delay and the steady state reached after the exponential decay. The data shown in figure 6.7 is recorded in a similar way to the bias curves previously shown. The tip is lifted by 1 nm, the feedback is turned off and a DC-bias is applied. With the feedback off, the delay between the two laser pulses is scanned and the change in frequency shift is recorded. Due to the tip-sample distance dependent frequency shift, any drift in the tip-sample distance will limit the maximum time during which the feedback can be turned off without encountering too many artifacts due to drift. This limits the integration time per delay setting at a given step size. To overcome these issues, a second measurement mode was therefore used, that allows for longer integration times.

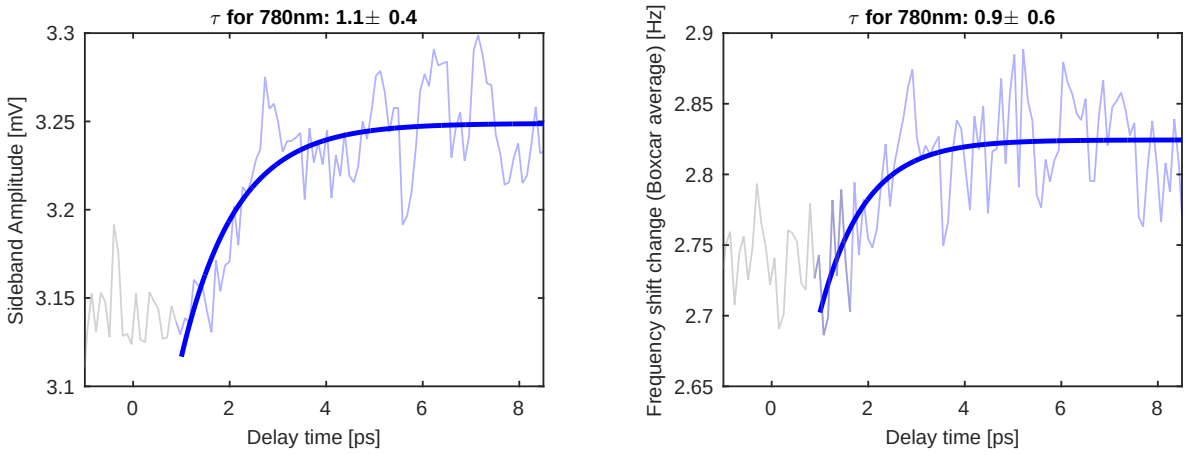

(a) (b)

Figure 6.7: Photocarrier decay measured in LT-GaAs without δF feedback. A 780 nm pump laser and a 610 nm probe laser is used. Decay time recording using the direct side band detection (a) compared to the boxcar averaging in the time domain (b) is shown. The decay is fitted to an exponential decay with a time constant of $\tau = 1.1 \pm 0.4$ ps for a) and $\tau = 0.9 \pm 0.6$ ps for b)

For the measurement shown in figure 6.8, the feedback was kept on, however, it was set to a very long time constant (>10 seconds). This is done to correct for any slow drifts without following the modulation due to the chopped laser illumination. To maximize the strength of the frequency shift modulation, a DC-bias is applied to the tip. The z-offset generated due to the additional bias, is compensated by a higher feedback setpoint to keep a constant tip-sample distance. The delay time between the laser is swept and the sideband, as well as the boxcar average, is recorded for each delay setting. Fitting of the decay data results in slightly higher decay times for the sideband ($\tau = 1.6 \pm 0.4$ ps) and for the boxcar averaging

($\tau = 1.6 \pm 0.8$ ps) compared to the constant height mode. These results however, are still within error compared to the previous measurement.

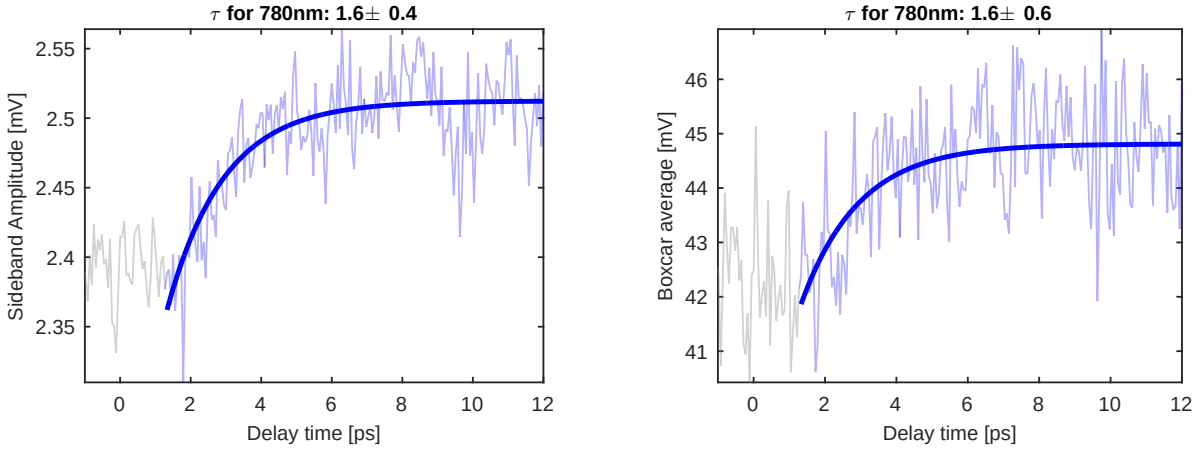

(a) (b)

Figure 6.8: Photocarrier decay measured in LT-GaAs. A 780 nm pump laser and a 610 nm probe laser is used. Decay time recording using the direct side band detection (a) compared to the boxcar averaging in the time domain (b). The decay is fitted with an exponential curve with a time constant of $\tau = 1.6 \pm 0.4$ ps for a) and $\tau = 1.6 \pm 0.6$ ps for b)

In general, the sideband detection appears to have a better signal-to-noise ratio due to the use of a lock-in measurement. Additionally, the sideband above $(f_0 + f_m)$ and the sideband below $(f_0 - f_m)$ the resonance frequency of the cantilever are added to increase the signal-to-noise ratio.

Since two lasers with different wavelengths are used in our pump-probe setup, we do not observe a symmetric behavior around zero delay which would be expected if the pump and

probe pulse were identical. We rather observe a wavelength-dependent characteristic decay depending on which pulse precedes. If the TVIS pulse (610nm) is delayed with respect to the 780 nm pulse, the decay of the 780 nm pulses excitation is measured. Therefore, for a negative delay time, the 610 nm pulse will precede the 780 nm pulse and the decay following the 610 nm pulse excitation is measured. Excitation around 780 nm is very close to the band gap of GaAs and should therefore only probe states within the central Γ-valley [81]. The 610 nm excitation carries additional energy and could therefore excited carriers into neighbouring valleys. The lifetimes for these states could be different. However, Schall et al. did not measure a significant difference between 800 nm and 400 nm pump wavelength measured by THz spectroscopy [81]. Additionally, as mentioned above, the intensity of the two pulses is not the same. Therefore, it is expected that the decay of the 610 nm pulse will exhibit a smaller change in the frequency shift. A scan from negative to positive delay times can be seen in figure 6.9. The positive delay time shows the decay of the 780 nm pulse (blue) and the negative delay time shows the decay of the 610 nm pulse (red). The decay following the 610 nm illumination corresponds to a longer lifetime.

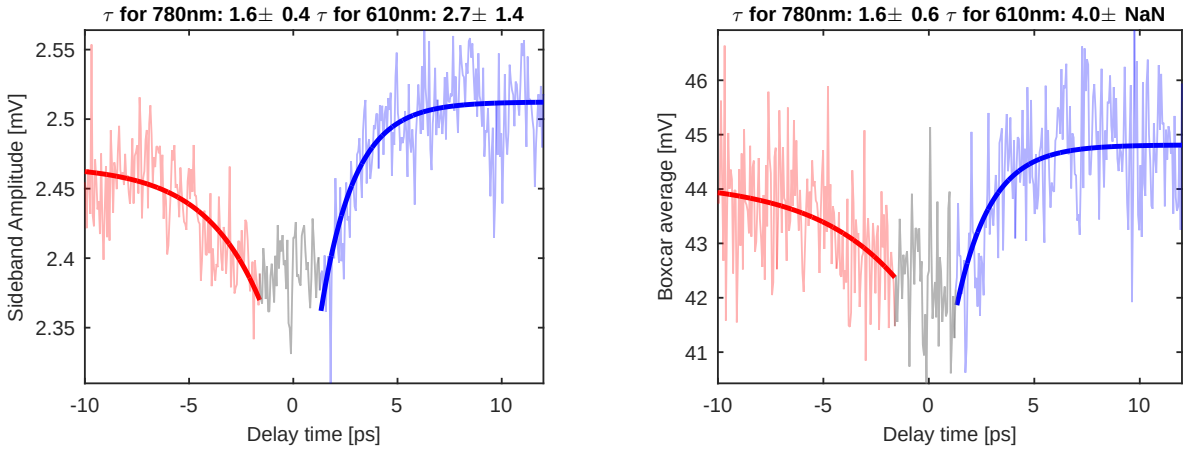

(a) (b)

Figure 6.9: Photocarrier decay measured in LT-GaAs without ΔF feedback. In red, the decay following the 610 nm pulse excitation is shown and in blue the decay following a 780 nm pulse illumination. The overall smaller amplitude of the 610 nm pulse decay is expected due to the lower average power of the laser at this wavelength.

6.4 Conclusion

We showed a novel analytical analysis of the ultimate lower limit in time constant measurements with AFM for a pump-probe style setup. This allows us to formulate the lower time limit of AFM in terms of the minimal measurable energy in AFM. We describe a pump-probe scheme with two excitation pulse trains delayed relative to each other that allow for non-linear decay time measurements limited by the thermal noise of the cantilever and not

the cantilever response time. Following the formulation of a lower time limit in terms of minimal energy, a measurement of the photocarrier lifetime in LT-GaAs is presented. For the first time, a decay time in the range of 1 ps was measured with AFM.

As mentioned in the introduction, this pump-probe type measurement is not limited to optical excitation. Any response which exhibits a non-linear decay can be measured using the described technique. A short pulse in the order of the decay times and delay time smaller than the decay constant are needed in order to resolve the decay time constants.

7

Conclusion and Outlook

Two new techniques are presented in this thesis to extend the reproducibility and time resolution of AFM measurements. The goal of these new techniques, as motivated in the introduction, is to have tools available for the measurement of photovoltaic samples under illumination.

First, a novel technique to measure the surface photovoltage under pulsed illumination with AFM is presented. It became evident that an improved method for the measurement of the surface photovoltage is needed since large variations of the surface photovoltage when measured over multiple hours were observed, as presented in chapter 3. Surface photovoltage is measured by subtracting the CPD measured under light illumination from a previous reference measurement under dark condition. This approach is ultimately limited by the stability of the contact potential difference between the tip and the sample. Hence, we

developed a time-domain KPFM technique (TD KPFM), a method which is not influenced by the long-term drift of the tip-sample potential. TD KPFM uses pulsed illumination to modulate the electrostatic force between two states, light on & light off. The modulation of the electrostatic force is then measured in the time-domain to extract the absolute values of the frequency shift. We use this modulation approach to measure a full Kelvin parabola (frequency shift-bias spectroscopy) of both states simultaneously. From the Kelvin parabola, we can extract information about the contact potential difference as well as information about the capacitance gradient. Any changes in the tip-sample potential occurring at a longer timescale than the light modulation will not influence the measured value. Therefore, the same surface photovoltage value can be measured over tens of hours while the traditional approach is influenced by any long-term drift. This was verified with a measurement of the surface photovoltage in silicon, as presented in chapter 5. TD KPFM yields a surface photovoltage (SPV) of 202±22 mV for 162 consecutive measurements over 18 hours while regular KPFM results in a SPV of 207±312 mV. This is a decrease of more than an order of magnitude in standard deviation.

We furthermore point out that the measured CPD by KPFM under pulsed illumination is no longer independent of the capacitance gradient. This can lead to an apparent shift in CPD since a change in CPD and capacitance gradient is expected upon illumination. This is an very important finding since many recent techniques are based on pulsed illumination

to measure the decay time with KPFM [66, 15]. We therefore conclude that any KPFM measurements under pulsed illumination should use a time-domain measurement approach like TD KPFM or at least monitor the capacitance gradient to verify any changes [74]. However, if regular KPFM with recording of the capacitance gradient is used, the measured CPD is still susceptible to drift in the tip-sample potential.

The reproducibility of surface photovoltage measurements by TD KPFM is a key step to be able to study the wavelength dependency. Wavelength dependent measurements take a long time due to the use of a discrete wavelength for each measurement. Hence, it is crucial to not be influenced by any long term drift of the tip-sample potential. Also, the measured surface photovoltage by TD KPFM is truly independent of the tip potential since only the change due to the illumination is measured. This allows for the comparison of measurements performed with different AFM tips and even allows for a comparison of absolute values acquired by different laboratories.

The second novel measurement technique developed and presented enables the measurement of ultrafast decay times by AFM, as shown in chapter 6. This measurement scheme was presented in a generic form to allow for the adaption to any modulated pump-probe sample excitation. In principle, this method can be used to measure any non-linear decaying tip-sample interactions. Key to this new method is the accurate measurement of an average force between a tip and a sample. In our experimental implementation of this new method,

we used ultrashort laser pulses (<100 fs) to generate an ultrafast photoconductive sample excitation. We demonstrate that optically measured ∼1ps decay times of this excitation can be measured by our ultrafast AFM technique. The AFM cannot resolve an individual ultrafast excitation event, it can, however, measure the average force. Our new method is thus an extension of classical ultrafast pump-probe methods replacing a slow electronic or optical detector with a mechanical detector with nanometer spatial resolution. Due to the localized tip-sample interaction, a high spatial resolution can be achieved, limited by the AFM setup and not the optical spot size. The key idea underpining this method is that when the signal of interest exhibits a non-linear nature, the average signal depends on the temporal spacing of the pulses. By delaying the probe pulses on the characteristic time scale of the phenomena being investigated, the average measured force is influenced. Since only the average interaction is measured, no modification to the existing mechanics or electronics of the AFM are needed. We established the lower limit of time resolution in AFM based on the thermal limit of AFM operation. Hence, the limiting factor is not how fast one can measure by AFM, but rather how small of a energy resolution can be achieved.

To illustrate such a pump-probe type measurement with a force readout by AFM, the photoexcitation decay time of ∼1ps of a low-temperature grown GaAs (LT-GaAs) sample was measured, as demonstrated in chapter 6.3. We used a pulsed laser illumination to excite carriers in LT-GaAs while measuring the average electrostatic force generated, using regular

fm-AFM. To implement this, a non-degenerate pump-probe setup was used with two lasers: a Toptica FemtoFiber Pro (780 nm, pulse width of <100 fs and average power of 29.8 mW, 80.1 MHz) and a Toptica FemtoFiber Pro TVIS (610 nm, pulse width of <400 fs and average power of 5.125 mW, 80.1 MHz). A decay time of the photocarriers of the LT-GaAs sample in the range of 1 ps was measured with AFM. This clearly demonstrates that ultrafast decay times can be measured with AFM and are not limited by the slow electronics or cantilever mechanics of the AFM. It is solely limited by the underlying physical process. This opens the door to measure local decay times rather than the average decay times measured over the size of the laser spot as the spatial resolution is given by the AFM. Even though we did not observe any spatial variation of the decay signal on our LT-GaAs sample, it is still a local measurement given by the nanometer spatial resolution of our AFM.

Outlook

The next step is to apply our new measurement techniques to thin film molecule samples in a UHV environment as outlined in the motivation of this thesis. An AFM image of pentacene and PTCDI adsorbed on KBr is shown in figure 7.1. It can be seen that due to the submonolayer coverage many different orientations between the two molecule islands exist on the sample. TD KPFM will lead to a more stable measurement of the surface photovoltage in organic thin film. However, applying this technique to a molecule sample can pose some

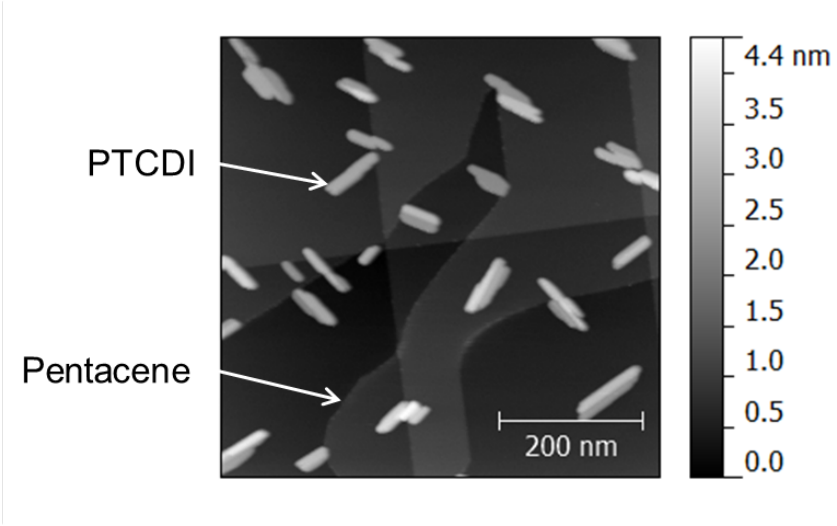

Figure 7.1: AFM image of pentacene and PTCDI adsorbed on KBr. Pentacene forms single monolayer flat islands, whereas PTCDI forms needle shaped islands. Such an arrangement of molecules would be a great sample to study the effect of molecule orientation on charge generation/separation.

additional challenges. We demonstrated the working principle of both measurement modes, TD KPFM and time resolution, for semiconductor samples. A thin film molecule sample will yield a smaller signal since less material is present. The number of excited carriers in our LT-GaAs decay measurement was estimated to be in the range of 10^{16} carriers per cm^3 based on the intensity used. The probe depth of KPFM is not yet well understood, however, it can range up to hundreds of nanometer into the substrate [45]. With a carrier density mentioned above and a spatial resolution of 10x10 nanometer with a probe depth of approximately 1μm (equal to 2/3 of the LT-GaAs layer), about 1 carriers are measured in our current case. One monolayer of molecules will have much fewer generated carriers. Following

the same assumption and a thickness of about 1 nm would result in only 10^{-3} carriers in the probe volume of KPFM. This illustrates the possible challenges for a measurement on organic thin films. This could be bypassed by longer averaging times, which, due to the use of TD KPFM developed in this thesis, can be very long as they are not limited by the tip-sample potential stability anymore. It will much rather be limited by the usual drift present in AFM measurements. Following the measurement of the surface photovoltage and decay times by TD KPFM, spatial mapping of such measurements could be of great interest. The illumination intensity used in our experiment can be increased, which should help to increase the intensity of the KPFM signal as well. With spatial resolved decay time measurements more insight into the charge generation process can be obtained. Due to the time resolution, it will be possible to distinguish between excitation, charge transfer states and separated charges. Spatial resolving the occurrence of these different states will allow to understand the structure-function relationship in more detail and the process of charge separation in general.

With respect to the time resolution measurement for optical excitation, it is worth mentioning that any sample that can be optically excited can now be studied with the spatial resolution of AFM. Even though OPV are the main focus for this technique in our group, it is not at all limited to it.

Further applications for the here presented novel techniques outside of pure optical stim-

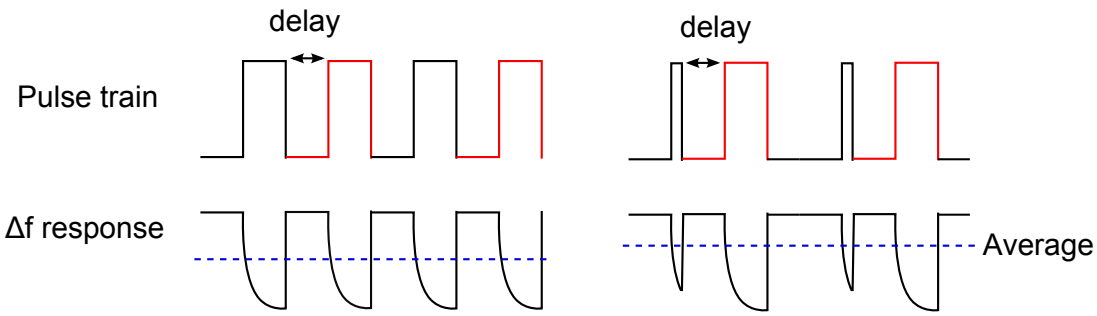

Figure 7.2: Conceptional drawing of time resolved measurement of ion movement in a sample measured by AFM. When the potential is stepped, ions will move to shield the electrical field, thus changing the capacitance and electrostatic force. A probe pulse (red) delayed relatively to a pump pulse (black) will result in a different average response when delayed within the non-linear decay of the signal.

ulation and photovoltaic research are also of great interest. The electrostatic force can be modulated not only by light illumination but also by other means. For example, the diffusion of ions in a sample will change the capacitance gradient of the electrostatic force [69]. This discharging of the sample capacitor follows an exponential decay as described by Schirmeisen [69]. Hence, the decay time of the signal due to the movements of ions could be measured by the pump-probe technique presented here. Figure 7.2 illustrates such a measurement. Two pulses delayed relative to each other will result in an average electrostatic force depending on the temporal distribution of the pulses, just like we showed with the optical excitation. Therefore, the average response can be used to extract the time constant of the non-linear decay. All one needs is to apply a train of two electric pulses of known pulse width and delay. The only difference is that the non-linear decay of the signal is not generated after

the pulse, but rather when the pulse is applied.

It should be noted that this measurement method is not limited to the modulation of the electrostatic force. Any signal which can be measured by AFM and can be externally modulated, can be used with the here presented novel approache.

Bibliography

[1] G. Binnig, C. F. Quate, and C. Gerber, "Atomic Force Microscope," *Physical Review Letters*, vol. 56, pp. 930–933, mar 1986.

[2] G. Binnig, H. Rohrer, C. Gerber, and E. Weibel, "Surface Studies by Scanning Tunneling Microscopy," *Physical Review Letters*, vol. 49, pp. 57–61, jul 1982.

[3] R. García, "Dynamic atomic force microscopy methods," *Surface Science Reports*, vol. 47, pp. 197–301, sep 2002.

[4] M. Nonnenmacher, M. P. O'Boyle, and H. K. Wickramasinghe, "Kelvin probe force microscopy," *Applied Physics Letters*, vol. 58, no. 25, p. 2921, 1991.

[5] L. Kelvin, "V. Contact electricity of metals," *Philosophical Magazine Series 5*, vol. 46, pp. 82–120, jul 1898.

[6] S. Sadewasser, "Experimental Technique and Working Modes," in *Kelvin Probe Force*

Microscopy (S. Sadewasser and T. Glatzel, eds.), vol. 48 of *Springer Series in Surface Sciences*, pp. 7–24, Berlin, Heidelberg: Springer Berlin Heidelberg, 2012.

[7] T. R. Albrecht, P. Grütter, D. Horne, and D. Rugar, "Frequency modulation detection using high-Q cantilevers for enhanced force microscope sensitivity," *Journal of Applied Physics*, vol. 69, p. 668, jan 1991.

[8] J. M. R. Weaver, "Semiconductor characterization by scanning force microscope surface photovoltage microscopy," *Journal of Vacuum Science & Technology B: Microelectronics and Nanometer Structures*, vol. 9, no. 3, p. 1562, 1991.

[9] D. C. Coffey and D. S. Ginger, "Time-resolved electrostatic force microscopy of polymer solar cells," *Nature Materials*, vol. 5, pp. 735–740, sep 2006.

[10] V. Palermo, M. Palma, and P. Samorì, "Electronic Characterization of Organic Thin Films by Kelvin Probe Force Microscopy," *Advanced Materials*, vol. 18, pp. 145–164, jan 2006.

[11] S. A. Burke, J. M. LeDue, J. M. Topple, S. Fostner, and P. Grütter, "Relating the Functional Properties of an Organic Semiconductor to Molecular Structure by nc-AFM," *Advanced Materials*, vol. 21, pp. 2029–2033, may 2009.

[12] S. Watanabe, Y. Fukuchi, M. Fukasawa, T. Sassa, A. Kimoto, Y. Tajima, M. Uchiyama, T. Yamashita, M. Matsumoto, and T. Aoyama, "In Situ KPFM Imaging of Local Pho-

tovoltaic Characteristics of Structured Organic Photovoltaic Devices," *ACS Applied Materials & Interfaces*, vol. 6, pp. 1481–1487, feb 2014.

[13] A. Henning, G. Günzburger, R. Jöhr, Y. Rosenwaks, B. Bozic-Weber, C. E. Housecroft, E. C. Constable, E. Meyer, and T. Glatzel, "Kelvin probe force microscopy of nanocrystalline TiO 2 photoelectrodes," *Beilstein Journal of Nanotechnology*, vol. 4, pp. 418–428, jul 2013.

[14] C. Loppacher, U. Zerweck, S. Teich, E. Beyreuther, T. Otto, S. Grafström, and L. M. Eng, "FM demodulated Kelvin probe force microscopy for surface photovoltage tracking," *Nanotechnology*, vol. 16, pp. S1–S6, mar 2005.

[15] G. Shao, M. S. Glaz, F. Ma, H. Ju, and D. S. Ginger, "Intensity-Modulated Scanning Kelvin Probe Microscopy for Probing Recombination in Organic Photovoltaics," *ACS Nano*, vol. 8, no. 10, pp. 10799–10807, 2014.

[16] H. Hoppe, T. Glatzel, M. Niggemann, A. Hinsch, M. C. Lux-Steiner, and N. S. Sariciftci, "Kelvin probe force microscopy study on conjugated polymer/fullerene bulk heterojunction organic solar cells.," *Nano letters*, vol. 5, pp. 269–74, feb 2005.

[17] F. Streicher, S. Sadewasser, and M. C. Lux-Steiner, "Surface photovoltage spectroscopy in a Kelvin probe force microscope under ultrahigh vacuum," *Review of Scientific Instruments*, vol. 80, no. 1, p. 013907, 2009.

[18] M. Wagner, Z. Fei, A. S. McLeod, A. S. Rodin, W. Bao, E. G. Iwinski, Z. Zhao, M. Goldflam, M. Liu, G. Dominguez, M. Thiemens, M. M. Fogler, A. H. Castro Neto, C. N. Lau, S. Amarie, F. Keilmann, and D. N. Basov, "Ultrafast and Nanoscale Plasmonic Phenomena in Exfoliated Graphene Revealed by Infrared Pum-Probe Nanoscopy," *Nano Letters*, vol. 14, pp. 894–900, feb 2014.

[19] S. Yoshida, Y. Terada, R. Oshima, O. Takeuchi, and H. Shigekawa, "Nanoscale probing of transient carrier dynamics modulated in a GaAs-PIN junction by laser-combined scanning tunneling microscopy," *Nanoscale*, vol. 4, no. 3, p. 757, 2012.

[20] J. Jahng, D. A. Fishman, S. Park, D. B. Nowak, W. A. Morrison, H. K. Wickramasinghe, and E. O. Potma, "Linear and Nonlinear Optical Spectroscopy at the Nanoscale with Photoinduced Force Microscopy," *Accounts of Chemical Research*, vol. 48, pp. 2671–2679, oct 2015.

[21] A. Köhler and H. Bässler, *Electronic Processes in Organic Semiconductors*. No. April, Weinheim, Germany: Wiley-VCH Verlag GmbH & Co. KGaA, may 2015.

[22] T. L. Benanti and D. Venkataraman, "Organic solar cells: an overview focusing on active layer morphology.," *Photosynthesis research*, vol. 87, pp. 73–81, jan 2006.

[23] K. a. Mazzio and C. K. Luscombe, "The future of organic photovoltaics," *Chem. Soc. Rev.*, vol. 44, no. 1, pp. 78–90, 2015.

[24] W. Cao and J. Xue, "Recent progress in organic photovoltaics: device architecture and optical design," *Energy & Environmental Science*, vol. 7, no. 7, p. 2123, 2014.

[25] J.-L. Bredas, "When Electrons Leave Holes in Organic Solar Cells," *Science*, vol. 343, pp. 492–493, jan 2014.

[26] J.-L. Brédas, J. E. Norton, J. Cornil, and V. Coropceanu, "Molecular Understanding of Organic Solar Cells: The Challenges," *Accounts of Chemical Research*, vol. 42, pp. 1691–1699, nov 2009.

[27] E. R. Bittner and C. Silva, "Noise-induced quantum coherence drives photo-carrier generation dynamics at polymeric semiconductor heterojunctions," *Nature Communications*, vol. 5, pp. 1–8, jan 2014.

[28] J.-L. Bredas, "Mind the gap!," *Materials Horizons*, vol. 1, no. 1, p. 17, 2014.

[29] Y. Yi, V. Coropceanu, and J.-L. Bredas, "Exciton-Dissociation and Charge-Recombination Processes in Pentacene/C 60 Solar Cells: Theoretical Insight into the Impact of Interface Geometry," *Journal of the American Chemical Society*, vol. 131, pp. 15777–15783, nov 2009.

[30] S. Gelinas, A. Rao, A. Kumar, S. L. Smith, A. W. Chin, J. Clark, T. S. van der Poll, G. C. Bazan, and R. H. Friend, "Ultrafast Long-Range Charge Separation in Organic Semiconductor Photovoltaic Diodes," *Science*, vol. 343, pp. 512–516, jan 2014.

[31] C. Silva, "Organic photovoltaics: Some like it hot.," *Nature materials*, vol. 12, pp. 5–6, jan 2013.

[32] J. Jahng, J. Brocious, D. a. Fishman, S. Yampolsky, D. Nowak, F. Huang, V. a. Apkarian, H. K. Wickramasinghe, and E. O. Potma, "Ultrafast pump-probe force microscopy with nanoscale resolution," *Applied Physics Letters*, vol. 106, p. 083113, feb 2015.

[33] Z. Schumacher, Y. Miyahara, L. Aeschimann, and P. Grütter, "Improved atomic force microscopy cantilever performance by partial reflective coating," *Beilstein Journal of Nanotechnology*, vol. 6, pp. 1450–1456, jul 2015.

[34] F. J. Giessibl, "Forces and frequency shifts in atomic-resolution dynamic-force microscopy," *Physical Review B*, vol. 56, pp. 16010–16015, dec 1997.

[35] U. Durig, "Relations between interaction force and frequency shift in large-amplitude dynamic force microscopy," *Applied Physics Letters*, vol. 75, no. 3, p. 433, 1999.

[36] A. E. Gildemeister, T. Ihn, C. Barengo, P. Studerus, and K. Ensslin, "Construction of a dilution refrigerator cooled scanning force microscope," *Review of Scientific Instruments*, vol. 78, p. 013704, jan 2007.

[37] F. J. Giessibl, "Principle of NC-AFM," in *Noncontat Atomic Force Microscopy* (S. Morita, F. J. Giessibl, and R. Wiesendanger, eds.), NanoScience and Technology, pp. 11–46, Berlin, Heidelberg: Springer Berlin Heidelberg, 2002.

[38] S. Kitamura and M. Iwatsuki, "High-resolution imaging of contact potential difference with ultrahigh vacuum noncontact atomic force microscope," *Applied Physics Letters*, vol. 72, no. 24, p. 3154, 1998.

[39] S. Sadewasser and M. C. Lux-Steiner, "Correct Height Measurement in Noncontact Atomic Force Microscopy," *Physical Review Letters*, vol. 91, p. 266101, dec 2003.

[40] P. Egberts, T. Filleter, and R. Bennewitz, "A kelvin probe force microscopy of charged indentation-induced dislocation structures in KBr," *Nanotechnology*, vol. 20, p. 264005, jul 2009.

[41] C. Barth and C. R. Henry, "Surface Double Layer on (001) Surfaces of Alkali Halide Crystals: A Scanning Force Microscopy Study," *Physical Review Letters*, vol. 98, p. 136804, mar 2007.

[42] J. L. Neff, P. Milde, C. P. León, M. D. Kundrat, L. M. Eng, C. R. Jacob, and R. Hoffmann-Vogel, "Epitaxial growth of pentacene on alkali halide surfaces studied by Kelvin probe force microscopy.," *ACS nano*, vol. 8, pp. 3294–301, apr 2014.

[43] U. Zerweck, C. Loppacher, T. Otto, S. Grafström, and L. M. Eng, "Accuracy and resolution limits of Kelvin probe force microscopy," *Physical Review B*, vol. 71, p. 125424, mar 2005.

[44] L. Gross, B. Schuler, F. Mohn, N. Moll, N. Pavliček, W. Steurer, I. Scivetti, K. Kotsis, M. Persson, and G. Meyer, "Investigating atomic contrast in atomic force microscopy and Kelvin probe force microscopy on ionic systems using functionalized tips," *Physical Review B*, vol. 90, p. 155455, oct 2014.

[45] O. A. Castañeda-Uribe, R. Reifenberger, A. Raman, and A. Avila, "Depth-Sensitive Subsurface Imaging of Polymer Nanocomposites Using Second Harmonic Kelvin Probe Force Microscopy," *ACS Nano*, vol. 9, pp. 2938–2947, mar 2015.

[46] G. Elias, T. Glatzel, E. Meyer, A. Schwarzman, A. Boag, and Y. Rosenwaks, "The role of the cantilever in Kelvin probe force microscopy measurements.," *Beilstein journal of nanotechnology*, vol. 2, pp. 252–60, jan 2011.

[47] S. Guriyanova, D. S. Golovko, and E. Bonaccurso, "Cantilever contribution to the total electrostatic force measured with the atomic force microscope," *Measurement Science and Technology*, vol. 21, p. 025502, feb 2010.

[48] L. Kronik, "Surface photovoltage phenomena: theory, experiment, and applications," *Surface Science Reports*, vol. 37, pp. 1–206, dec 1999.

[49] L. Kronik and Y. Shapira, "Surface photovoltage spectroscopy of semiconductor structures: At the crossroads of physics, chemistry and electrical engineering," *Surface and Interface Analysis*, vol. 31, no. 10, pp. 954–965, 2001.

[50] D. K. Schroder, "Surface voltage and surface photovoltage: history, theory and applications," *Measurement Science and Technology*, vol. 12, pp. R16–R31, mar 2001.

[51] L. Barnea-Nehoshtan, S. Kirmayer, E. Edri, G. Hodes, and D. Cahen, "Surface Photovoltage Spectroscopy Study of Organo-Lead Perovskite Solar Cells," *The Journal of Physical Chemistry Letters*, vol. 5, pp. 2408–2413, jul 2014.

[52] F. Fuchs, F. Caffy, R. Demadrille, T. Mélin, and B. Grévin, "High-Resolution Kelvin Probe Force Microscopy Imaging of Interface Dipoles and Photogenerated Charges in Organic Donor-Acceptor Photovoltaic Blends," *ACS Nano*, vol. 10, pp. 739–746, jan 2016.

[53] M. Beu, K. Klinkmüller, and D. Schlettwein, "Use of Kelvin probe force microscopy to achieve a locally and time-resolved analysis of the photovoltage generated in dye-sensitized ZnO electrodes," *Physica Status Solidi (a)*, vol. 211, pp. 1960–1965, sep 2014.

[54] F. Fuchs, M. Linares, C. de Vet, P. Leclère, R. Demadrille, and B. Grévin, "On the Photo-Induced Charge-Carrier Generation within Monolayers of Self-Assembled Organic Donor-Acceptor Dyads.," *Advanced materials (Deerfield Beach, Fla.)*, vol. 26, pp. 6416–6422, oct 2014.

[55] L. Howald, H. Rudin, and H.-J. Guntherodt, "Piezoelectric inertial stepping motor with spherical rotor," *Review of Scientific Instruments*, vol. 63, no. 8, p. 3909, 1992.

[56] L. Gross, F. Mohn, N. Moll, P. Liljeroth, and G. Meyer, "The Chemical Structure of a Molecule Resolved by Atomic Force Microscopy," *Science*, vol. 325, pp. 1110–1114, aug 2009.

[57] R. Bennewitz, "Structured surfaces of wide band gap insulators as templates for overgrowth of adsorbates," *Journal of Physics: Condensed Matter*, vol. 18, pp. R417–R435, jul 2006.

[58] D. Nabok, P. Puschnig, C. Ambrosch-Draxl, O. Werzer, R. Resel, and D.-M. Smilgies, "Crystal and electronic structures of pentacene thin films from grazing-incidence x-ray diffraction and first-principles calculations," *Physical Review B*, vol. 76, p. 235322, dec 2007.

[59] S. A. Burke, J. M. Topple, and P. Grutter, "Molecular dewetting on insulators," *Journal of Physics: Condensed Matter*, vol. 21, no. 42, p. 423101, 2009.

[60] W. Paul, Y. Miyahara, and P. Grütter, "Implementation of atomically defined field ion microscopy tips in scanning probe microscopy," *Nanotechnology*, vol. 23, p. 335702, aug 2012.

[61] H. Sakaguchi, F. Iwata, A. Hirai, A. Sasaki, and T. Nagamura, "Nanometer-Scale Photoelectric Property of Organic Thin Films Investigated by a Photoconductive Atomic

Force Microscope," *Japanese Journal of Applied Physics*, vol. 38, pp. 3908–3911, jun 1999.

[62] D. C. Coffey, O. G. Reid, D. B. Rodovsky, G. P. Bartholomew, and D. S. Ginger, "Mapping Local Photocurrents in Polymer/Fullerene Solar Cells with Photoconductive Atomic Force Microscopy," *Nano Letters*, vol. 7, pp. 738–744, mar 2007.

[63] I. Beinik, M. Kratzer, A. Wachauer, L. Wang, Y. P. Piryatinski, G. Brauer, X. Y. Chen, Y. F. Hsu, A. B. Djurišić, and C. Teichert, "Photoresponse from single upright-standing ZnO nanorods explored by photoconductive AFM," *Beilstein Journal of Nanotechnology*, vol. 4, pp. 208–217, mar 2013.

[64] A. M. Goodman, "A Method for the Measurement of Short Minority Carrier Diffusion Lengths in Semiconductors," *Journal of Applied Physics*, vol. 32, no. 12, p. 2550, 1961.

[65] E. O. Johnson, "Measurement of Minority Carrier Lifetimes with the Surface Photovoltage," *Journal of Applied Physics*, vol. 28, no. 11, p. 1349, 1957.

[66] M. Takihara, T. Takahashi, and T. Ujihara, "Minority carrier lifetime in polycrystalline silicon solar cells studied by photoassisted Kelvin probe force microscopy," *Applied Physics Letters*, vol. 93, no. 2, p. 021902, 2008.

[67] L. Borowik, H. Lepage, N. Chevalier, D. Mariolle, and O. Renault, "Measuring the lifetime of silicon nanocrystal solar cell photo-carriers by using Kelvin probe force mi-

croscopy and x-ray photoelectron spectroscopy," *Nanotechnology*, vol. 25, p. 265703, jul 2014.

[68] T. Hochwitz, A. K. Henning, C. Levey, C. Daghlian, J. Slinkman, J. Never, P. Kaszuba, R. Gluck, R. Wells, P. John, and R. Finch, "Imaging integrated circuit dopant profiles with the force-based scanning Kelvin probe microscope," *Journal of Vacuum Science & Technology B: Microelectronics and Nanometer Structures*, vol. 14, p. 440, jan 1996.

[69] A. Schirmeisen, A. Taskiran, H. Fuchs, B. Roling, S. Murugavel, H. Bracht, and F. Natrup, "Probing ion transport at the nanoscale: Time-domain electrostatic force spectroscopy on glassy electrolytes," *Applied Physics Letters*, vol. 85, no. 11, p. 2053, 2004.

[70] F. Menges, H. Riel, A. Stemmer, C. Dimitrakopoulos, and B. Gotsmann, "Thermal Transport into Graphene through Nanoscopic Contacts," *Physical Review Letters*, vol. 111, p. 205901, nov 2013.

[71] R. J. Hamers and D. G. Cahill, "Ultrafast time resolution in scanned probe microscopies," *Applied Physics Letters*, vol. 57, no. 19, pp. 2031–2033, 1990.

[72] R. J. Hamers and D. G. Cahill, "Ultrafast time resolution in scanned probe microscopies: Surface photovoltage on Si(111)-(7x7)," *Journal of Vacuum Science & Technology B: Microelectronics and Nanometer Structures*, vol. 9, p. 514, mar 1991.

[73] D. P. E. Smith, "Limits of force microscopy," *Review of Scientific Instruments*, vol. 66, no. 5, p. 3191, 1995.

[74] Z. Schumacher, Y. Miyahara, A. Spielhofer, and P. Grutter, "Measurement of Surface Photovoltage by Atomic Force Microscopy under Pulsed Illumination," *Physical Review Applied*, vol. 5, no. 4, p. 044018, 2016.

[75] S. Gupta, M. Y. Frankel, J. A. Valdmanis, J. F. Whitaker, G. A. Mourou, F. W. Smith, and A. R. Calawa, "Subpicosecond carrier lifetime in GaAs grown by molecular beam epitaxy at low temperatures," *Applied Physics Letters*, vol. 59, no. 25, p. 3276, 1991.

[76] G. Segschneider, F. Jacob, T. Löffler, H. G. Roskos, S. Tautz, P. Kiesel, and G. Döhler, "Free-carrier dynamics in low-temperature-grown GaAs at high excitation densities investigated by time-domain terahertz spectroscopy," *Physical Review B*, vol. 65, p. 125205, mar 2002.

[77] E. S. Harmon, M. R. Melloch, J. M. Woodall, D. D. Nolte, N. Otsuka, and C. L. Chang, "Carrier lifetime versus anneal in low temperature growth GaAs," *Applied Physics Letters*, vol. 63, no. 16, p. 2248, 1993.

[78] G. Jellison, "Optical functions of GaAs, GaP, and Ge determined by two-channel polarization modulation ellipsometry," *Optical Materials*, vol. 1, pp. 151–160, sep 1992.

[79] A. a. Milner, K. Zhang, V. Garmider, and Y. Prior, "Heating of an Atomic Force Microscope tip by femtosecond laser pulses," *Applied Physics A*, vol. 99, pp. 1–8, apr 2010.

[80] K. a. McIntosh, K. B. Nichols, S. Verghese, and E. R. Brown, "Investigation of ultrashort photocarrier relaxation times in low-temperature-grown GaAs," *Applied Physics Letters*, vol. 70, no. 3, p. 354, 1997.

[81] M. Schall, M. Walther, C. Winnewisser, H. Helm, and P. U. Jepsen, "Subpicosecond time-resolved terahertz time-domain spectroscopy of transient carrier dynamics in semiconductors," in *SPIE/EOS International Symposium on Terahertz Radiation* (J. M. Chamberlain, ed.), pp. 220–227, sep 1999.